

Thermodynamic modeling framework for prediction of tool wear and tool protection phenomena in machining

Axel Bjerke^{a,*}, Andrii Hrechuk^a, Filip Lenrick^a, Andreas Markström^b, Henrik Larsson^c, Susanne Norgren^d, Rachid M'Saoubi^e, Thomas Björk^f, Volodymyr Bushlya^a

^a Division of Production and Materials Engineering, Lund University, Ole Römers väg 1, Lund, Sweden

^b Thermo-Calc Software AB, Råsundavägen 18, SE-169 67, Solna, Sweden

^c Unit of Structures, Dept Materials Science and Engineering, KTH, SE-10044, Stockholm, Sweden

^d Sandvik R&D, Lerkrogsv. 13, 126 80, Stockholm, Sweden

^e R&D Materials and Technology Development, Seco Tools AB, 737 82, Fagersta, Sweden

^f Ovako Group, Olof Hjorts väg 2, 813 35, Hofors, Sweden

ARTICLE INFO

Keywords:

Wear modelling
Thermodynamic modeling
Steel
Ultra-hard materials
Cutting tools
Electron microscopy

ABSTRACT

Chemical, oxidation and diffusional interactions between the tool, chip and cutting environment are known tool wear mechanisms in machining. However, the interaction between tool, coating, workpiece, coolant and atmospheric oxygen can, under favorable conditions, lead to formation of reaction products that retard tool wear. A method with the ability to predict these interactions, would therefore enable a better control over tool life in machining. An attempt to create such a modelling framework is developed in this study. This method can predict the phase composition and the driving force for degradation and the formation of protective interaction products in the cutting zone. This modeling approach is applicable across cutting processes in which chemical, diffusional and oxidation wear are dominant or present. This framework has been applied to investigate the interactions occurring in the cutting zone during turning of a medium alloyed low-carbon steel (Hybrid Steel® 55). A range of degradation events are predicted, as well as the formation of a protective corundum $(\text{Al},\text{Fe},\text{Cr})_2\text{O}_3$ or spinel $(\text{Al},\text{Fe},\text{Cr})_3\text{O}_4$ film due to an interaction between the Al-alloyed steel and the environment. Validation of the modeling was performed by studying tool wear and reaction products formed when machining with ceramics, PCBN and coated carbide tooling. Inserts are studied by the use of scanning and transmission electron microscopy, after cutting tests were performed. Additional tests were performed in different environments (dry, argon and coolant). The results confirmed the model predictions of oxidation and diffusion wear as well as the formation of an $(\text{Al},\text{Fe},\text{Cr})_3\text{O}_4$ tool protection layer. Thus, the proposed thermodynamic framework seem promising to serve as a predictive instrument for the correct pairing of existing tool and workpiece combinations and cutting parameters, or for tailoring respective material compositions for intentional formation of a tool protection layer. As well as guidance on how to apply present and future kinetic models when concurrent interaction mechanisms are present. Which lead to a reduction and minimization of costly experimental machining tests.

1. Introduction

Predictive models of metal cutting are an essential tool to reach optimum productivity [1]. Tool life modelling originated with the development of Taylor's equation [2] which relates the cutting speed to the tool life, and was later extended by Colding to include an equivalent chip thickness [3]. These equations and their derivatives are empirical models describing tool life expectancy for a narrow window of process conditions and materials. These models are routinely used in industry

[4], despite their heavy reliance on large arrays of repetitive experimental data and absence of relations to occurring physical phenomena.

The limitations of empirical models were recognized early and this lead to the interest in physics-based analytical tool wear models, designed to have a predictive power independently of process conditions. One of the earliest models is the abrasive wear model by Archard [5] operating with the single wear mechanism of abrasion. Similar single-mechanism models predicting the kinetics of tool wear by diffusion [6,7] and thermodynamic models of the chemical interactions [8]

* Corresponding author.

E-mail address: axel.bjerke@iprod.lth.se (A. Bjerke).

are among the original attempts to model tool wear. However, it should be recognized that many such models are physics-based but not entirely analytical, because they rely on experimental cutting data to calibrate the underlying equations.

Modern high-speed machining generates high temperatures in the cutting zone, which activate multiple interdependent wear mechanisms, such as chemical, oxidative and diffusional wear [9]. These multiple and interdependent wear mechanism cannot be modeled by the early single wear mechanism models. This problem motivated the development of hybrid models build-up of multiple single wear mechanisms models with assumed weight coefficients. Kramer and von Turkovich [10] combined abrasive and dissolution wear models into a composite model and proposed a series machining procedures to estimate the weightings. Huang and Dawson [11] further extended this approach to combine three mechanisms of abrasion, adhesion and diffusion for the case of P_cBN wear in hard turning. Malakizadi et al. [12] developed a thermodynamics approach to assess the potential solubility of W and C in the steel for uncoated tools. This model was further combined with finite element (FEM) simulations to map process temperature for a range of cutting data and tool wear. Empirical coefficients were then used to transform the calculated potential solubility at the modeled temperature into tool material loss.

Unfortunately, the tool life determining wear mechanisms are not known before conducting a machining test. Thus, an accurate assignment of weight coefficients for each of the mechanisms or even predicting what mechanism will occur, is not possible before a machining test and its rigorous analysis has been conducted. The predictive power of such hybrid models are consequently limited, because each unique combination of cutting data and conditions, will affect such weightings in their unique way. At the same time, current kinetic and analytical models are unable to handle concurrent wear mechanisms for multi-component interaction systems. Hence, a model that can predict the tool life determining wear mechanisms is needed for degradation driven by thermodynamics and chemistry in addition to mechanical wear. Either to reduce the complexity the modeling problem to be able to develop completely analytical kinetic models or to analytically predict the weighing coefficients, before cutting tests are carried out.

Further complications, even for single-mechanism modeling, can arise when the interaction between tool and workpiece or environment does not lead to tool degradation. Interactions have shown to result in the build-up of tool protective layers and reaction products retarding tool wear. Gutnichenko et al. [13] demonstrated the formation of an Al₂O₃ film on P_cBN tools while machining white cast iron, which resulted in suppressed crater wear, thereby acting as a tool protection layer (TPL). A tool protection layer differs from well-known mechanisms such as built-up layers (BUL), transfer layers (TL), tribofilms [14] or deformed binder material [15]. A TPL represents a new phase that is formed on the surface of the tool *in-operando*, due to the reaction between the tool, cutting environment and workpiece [16]. The formation of such a TPL has been reported for tool and workpiece interaction in which NbC [17], (Ti,V)C or (Ti,V,Cr)B₂ [18], (Ti,Nb)N [19] and (bcc) W [20] films formed during the cutting process. Experimental observations have also reported on the formation of Al₂O₃ [21], Al-O and AlN [22] as a result of interaction between the tool and workpiece as well as atmospheric air. The understanding and predictive modeling of the TPL formation and its stability is absent in literature, despite the benefits of retarding tool wear that are offered by a tool protection layer. Not being able to predict the formation and stability of TPLs hinders the correct pairing of existing tool and workpiece material, or the tailoring of material compositions and machining parameters for the intentional formation of build-up of such a protection layer.

This study develops a modeling framework based on thermodynamic calculations, which act as a predictive instrument for chemical, thermal, oxidative and diffusional interactions in machining. This is in contrast to works using thermodynamic modeling to describe and rank degradation mechanism based on experiments results [23,24], rather than

predicting it. This modeling framework has also been developed to predict the potential formation of a tool protection layers in addition to degradation and the conditions for its existence and stability.

Hence, this method predicts which phenomena will occur, their driving forces and provides an assessment of their relative importance. However, it is not capable of predicting the rate at which the mechanisms will result in degradation or protection. Rates are predicted by kinetic models, which currently cannot model the concurrent multi-component interaction system of metal cutting without empiric fitting. However this model's predictive power can reduce the complexity of the wear process, to potentially allow current analytical and kinetic models to be used without empirical fitting. The proposed thermodynamic predictive framework has been exemplified and validated for machining a medium alloy low-carbon steel (Hybrid Steel® 55) using six tool materials. The validation has also been supported by scanning and transmission electron microscopy, infrared thermography and cutting tests in different environments (dry, argon and coolant). The results demonstrate how the thermodynamic model can currently be used to select tool materials, alloying compositions and cutting parameters that lead to the formation of tool protection layers. While also potentially reducing the reliance on empirical fitting parameters, when applying kinetic models.

2. Methods

The thermodynamic and chemical interactions during the cutting process involves close contact between a cutting tool and a workpiece in a specific environment. Such interactions can be divided into three individual categories (i–iii) or their combination (iv). (Fig. 1):

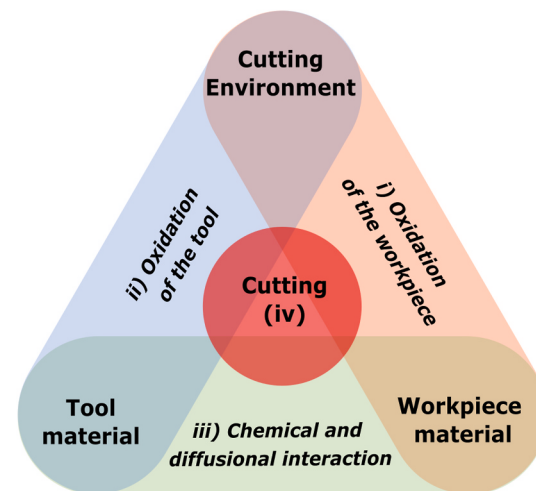


Fig. 1. Schematic illustration showing three individual interactions (corners), their interplay during the cutting process (sides) and their combined effect (center).

ii) Oxidation of the tool material. The tool material itself can react with atmospheric oxygen or oxygen in the workpiece during the cutting process, which may lead to the formation of softer, deformable or even vaporizable oxides, all of which can result in rapid tool degradation [27]. The rate of oxidation depends on the process temperature, contact pressure, material system and the availability of oxygen during the cutting process [28].

iii) Chemical and diffusional interaction. The tool and the workpiece can also react or dissolve by diffusion into each other, leading to chemical [29] and diffusional wear mechanisms [30]. The pressure, temperature and composition of the tool and workpiece materials will determine the possibility and rate of such reactions [12].

iv) The cutting process. The above three interactions: oxidation of the workpiece (i), oxidation of the tool (ii) and chemical and diffusional interaction (iii) frequently occur concurrently in the cutting process. However, the cutting process may also involve an extra layer of interactions, such as the interaction between the tool and workpiece oxides formed *in-operando*.

i) Oxidation of the workpiece material. The workpiece itself, the generated chips and workpiece material adhered to the tool, can react with oxygen from the environment. This phenomenon leads to formation of oxides which, in turn, can protect the tool from oxidation [22,25], or react with the tool and accelerate the degradation of the tool material [26].

There are currently several categories of models, and their development is briefly outlined in the Introduction (Section 1). They may be divided into empirical models that rely on technological variables such as cutting speed, feed, depth of cut and tool geometry [4]. There are early physics-based models that describe a single mechanism [7,31]. Then there are hybrid models that combine analytical models with empirical coefficients [10,12,29]. Finally there are analytical models based on only thermodynamics and kinetics which are used to describe the observed phenomenon [17,23,24,32].

The framework developed in this paper (Fig. 1) is an analytical model based on thermodynamics. This relies on the physical quantities such as temperature, pressure and chemical potential, as outlined in Section 2.1 and Appendix A, this makes it possible to create predictive results before any machining tests are performed, regarding the thermal and chemical wear. This allows for predicting protective interaction phenomena, which models found in literature have not attempted to do.

2.1. Computational framework

CALPHAD is a phenomenological approach for calculating thermodynamic, kinetic, and other properties of multicomponent materials systems. It is based on describing the properties of the fundamental building blocks of materials, namely the phases, starting from pure elements and binary and ternary systems. CALPHAD predicts the properties of higher order alloys, with extrapolation from the binary and ternary systems. Over the last decades, the CALPHAD method has successfully been used for development of numerous engineering materials. It has also been used to study and describe different types of tool – workpiece interactions, see e.g. Refs. [17,32], however it has not to the authors' knowledge been used to create generic tool wear models.

In CALPHAD the Gibbs energy (G^α) of each phase ($\alpha, \beta \dots$) is described as a function of pressure (P), temperature (T) and composition (x_i^α). The thermodynamic modeling of Gibbs energy is based on physical models and is described in Appendix 1. Gibbs energy is chosen since in an isothermal isobaric system, equilibrium is reached when the Gibbs energy reaches its minimal value. The current study uses Thermo-Calc [33], a CALPHAD-based software. This method can calculate all the thermodynamic properties of the system at a given composition (X_i), temperature (T) and pressure (P).

Thus, the task is to translate the cutting parameters into thermodynamic quantities. The physical state (P, T, X_i) in the cutting zone depend on cutting parameters such as cutting speed (v_c), feed (f), depth of cut (a_p), materials, tool geometry, etc. It should also be noted that conditions vary across the tool/chip and tool/workpiece contact zones. The contact pressures can reach above 10^9 Pa and temperatures often range from 500 °C to 1300 °C [34,35]. The availability of oxygen in the cutting zone, is in this paper expressed using the oxygen activity where the reference state is pure oxygen gas; the oxygen activity thus correspond to the partial pressure of O_2 (dimensionless), it is 1 in a pure O_2 environment, approximately 0.21 in the ambient atmosphere and 0 in an oxygen-free environment. Hence, a partial pressure in the range of 0–0.21 is expected across the seizure zone, sliding zone and transition zone [36]. The state will also in general change during the cutting process. The tool will initially encounter a continuous supply of workpiece material, but adhered metal or a reaction product might also separate the tool from the chip and workpiece as the cutting progresses. The effect of any change in the composition and cutting parameter space can therefore be explored before any cutting tests are executed. Thus predict the formation of different reaction products at the tool/chip

interface assuming that all phases have equal nucleation energy e.g. disregarding the kinetics of the reactions.

The above translation allows us to calculate the equilibrium phase composition ($x_i^\alpha, x_i^\beta \dots$) in the cutting zone (Eq. (1)). The calculation results show if the tool material is thermodynamically stable at elevated process temperatures and pressures. The result also give the equilibrium phase composition in the cutting zone. These results then indicate what phases will form in the cutting zone.

$$G(P, T, X_i, \dots) = G^\alpha(P, T, x_i^\alpha, \dots) + G^\beta(P, T, x_i^\beta, \dots) + \dots \quad (1)$$

This also allows the normalized driving force per mole (dimensionless) for the precipitation of these reaction products to be calculated. To do this, the phase composition of the tool, workpiece and the environment are first defined, then followed by the equilibrium state calculations. It is then possible to obtain the driving force for the formation of the first infinitesimal amount of reaction products, for the given equilibrium state. This allows the driving forces to be evaluated independently of any conceivable reaction products. The driving force for phases likely to form defined by the initial equilibrium calculations (Equation (1)) are shown in the results, however the driving force of any other phase can also be calculated using this method.

Consequently, careful translation of the cutting conditions into thermodynamic boundary conditions is crucial because correct translation makes it possible to calculate whether the tool and workpiece materials are stable or will react with each other or the environment (interactions i–iv). The equilibrium phase composition and the driving force for the reaction products to be formed can then be calculated and identified, if a reaction occurs. These procedural steps are performed for the given boundary conditions of temperatures, pressures, cutting environments, tools and workpiece combinations.

2.2. Experimental framework

The above-described methodology of investigating the interactions between tool, workpiece and the environment during metal cutting is independent of the materials, tool and cutting parameters in question. The selected material for this particular machining test is Hybrid Steel® 55 (X20NiCrAlMoV6-5-2-1), a medium alloy low-carbon steel. Hybrid Steel® 55 alloyed with Mn, Cr, Ni, Mo, V and Al according to Table 1. This kind of alloying should allow for a wide range of potential interactions.

Machining was performed for the steel supplied in a quenched and aged condition, which resulted in a microstructure of tempered martensite, fine carbides and precipitates of a Ni_3Al intermetallic phase. Fig. 2a is the X-ray diffraction (XRD) spectrum indicate the presence of tempered martensite and the Ni_3Al phase. Fig. 2b shows the backscatter electron (BSE) image of the material displaying a martensitic lath structure. The Vickers hardness of aged steel is measured to $HV10 = 4.8$ GPa.

The machining was longitudinal finish turning on a CNC SMT500 lathe (70 kW) at a constant cutting speed of $v_c = 300$ m/min, feed $f = 0.1$ mm/rev and depth of cut of $a_p = 0.3$ mm under dry cutting conditions. Through an iterative increase in cutting speed, these test conditions were found to provide sufficient tool life for investigation of wear processes and reflect an actual production viewpoint.

Six different tool materials (Table 2) were tested to investigate the machinability of the steel and to explore the widest range of interactions. The tools were a titanium aluminum nitride ((Ti,Al)N) physical vapor deposition (PVD) coated cemented carbide (WC-Co), four ceramic tools and a polycrystalline cubic boron nitride (PcBN) with low cBN concentration (50 vol %) and TiC binder. The four ceramic tools among which three contained silicon-based phases were silicon nitride (Si_3N_4), $SiAlON$, and whisker-reinforced alumina ($Al_2O_3-SiC_w$). The fourth ceramic tool is a mixed alumina (Al_2O_3-TiC). This choice of workpiece and tool material is selected to allow for the studying of

Table 1

Hybrid Steel® 55 composition by wt. % [48].

	C	Si	Mn	P	Cr	Ni	Mo	V	Al	Fe
Min (mass %)	0.16	0	0.20	0	4.80	5.80	0.60	0.45	2.00	balance
Max (mass %)	0.20	0.20	0.40	0.015	5.20	6.20	0.80	0.55	2.40	

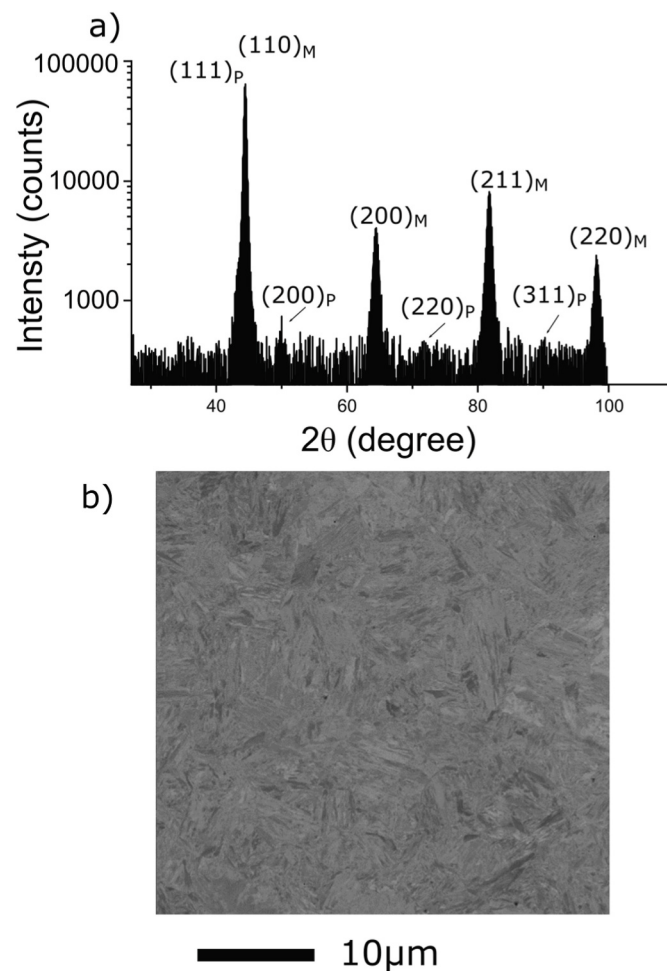


Fig. 2. a) XRD spectrum showing tempered martensite (M) and Ni_3Al precipitates (P) and b) backscatter image (BSE) of the martensitic lath structure of aged Hybrid Steel® 55 precipitates.

Table 2

List of tools materials and geometry.

Tool material	Geometry
WC-Co (substrate), (Ti,Al)N (coating)	CNMG120408-MF1
Si_3N_4 (solid ceramic)	CNGA120408T02020
$\text{Al}_2\text{O}_3 \cdot \text{SiC}_w$ (whisker reinforced ceramic)	CNGA120408T0120
SiAlON (solid ceramic)	CNGA120408E
$\text{Al}_2\text{O}_3 \cdot \text{TiC}$ (mixed ceramic)	CNGA120408T00520
50% cBN (grains) and TiC (binder)	CNGA120408S-01020-L1-U

several types of chemical and thermodynamic interactions, rather than abrasive wear.

The machining test was initially conducted at intervals of 15 s. However, longer intervals were used for higher preforming tools ($\text{Al}_2\text{O}_3\text{-TiC}$ and cBN-TiC). The cutting test was used to measure wear development, tool life and investigate interaction mechanisms. All cutting tests were also repeated for every tool at an engagement time exceeding the tools obtained tool life. Flank wear, rake wear and cutting

forces were continuously measured. Flank wear measurements were performed using an Olympus SZX7 stereo light optical microscope, while an Alicona Infinite Focus 3D microscope was used for crater wear analysis. The wear criteria were set to flank wear $VB = 200 \mu\text{m}$ due to the tolerances needed for finish machining of bearing steel and the crater wear criteria was set to $KT = 30 \mu\text{m}$ due to the risk of tool breakage. A PCLNL2525M12 tool holder was used and the cutting forces was monitored using a Kistler 9129AA dynamometer.

Worn tools were investigated using a Tescan Mira3 Scanning Electron Microscope (SEM), with both secondary (SE) and backscatter electron (BSE) detectors. It is also equipped with an X-ray Energy Dispersive Spectrometer (XEDS), used in this study to investigate the elemental composition. Focused ion beam (FIB) samples for transmission electron microscopy (TEM) were extracted from the tools using a FEI Nova NanoLab 600 FIB-SEM. A JEM-3000F TEM, also equipped with an XEDS, this was used to investigate the chemical and phase composition of worn tools and interaction products.

3. Results and discussion from the theoretical prediction

The results from the thermodynamic predictions are given in this section. The results are grouped into the oxidation of the workpiece material (*interaction i*) in 3.1, the oxidation of the tool materials (*interaction ii*) in 3.2, the chemical and diffusional interaction (*interaction iii*) and the overall cutting process (*iv*) in 3.3. Section 3.1, 3.2 and 3.3 are further divided in the following tool material categories: 1. Silicon containing tools (Si_3N_4 , $\text{Al}_2\text{O}_3\text{-SiC}_w$, SiAlON), 2. The coated cemented carbide tool ((Ti,Al)N coated WC-Co) and 3. Titanium carbide containing tools ($\text{Al}_2\text{O}_3\text{-TiC}$, cBN-TiC).

3.1. Oxidation of workpiece material (*i*)

The equilibrium phase composition was modeled at different pressures, temperatures and effective O_2 partial pressures (see Fig. 3a). This creates the possibility of mapping the physical quantities of machining parameters to specific areas of the cutting zone. This modeling section aims to illustrate and predict potential oxides that might form in the cutting zone as a result of a reaction between the workpiece material and the environment. The results in this section show all phases that are thermodynamically stable under the prevailing conditions, for reactions in category *i* *oxidation of the workpiece*. The calculations were performed for temperatures from 25 °C and up to 1200 °C, for pressures from 10^5 Pa up to 10^9 Pa and from an effective O_2 partial pressure of 0–0.21. For ease of comparison, all figures were plotted at 1000 °C and 10^5 Pa as these conditions were found to be most illustrative. Additional figures and comments are introduced when a change in temperature and pressure results in a significant change in the behavior of the interaction. The databases contain information about molar volume, but not its volume dependence on pressure, which is a good approximation of these phases when the pressure is below 10^9 Pa [37]. Gases such as Ar, O_2 and CO_2 is modeled as one phase (gas) with different constituents (Ar, O_2 , CO_2 etc.).

Fig. 3a reports the equilibrium phase fraction as a function of the effective O_2 partial pressure at 1000 °C and 10^5 Pa for Hybrid Steel® 55. FCC (austenite) is the equilibrium phase of the steel at this temperature and pressure. Fig. 3b gives the driving force for the formation of these oxides from a gas (Ar and O_2) and Hybrid Steel® 55, versus increasing effective partial pressure of O_2 at 1000 °C and 10^5 Pa . Fig. 3 reports the modeling results which predict that $(\text{Al},\text{Fe},\text{Cr})_2\text{O}_3$ mixed corundum

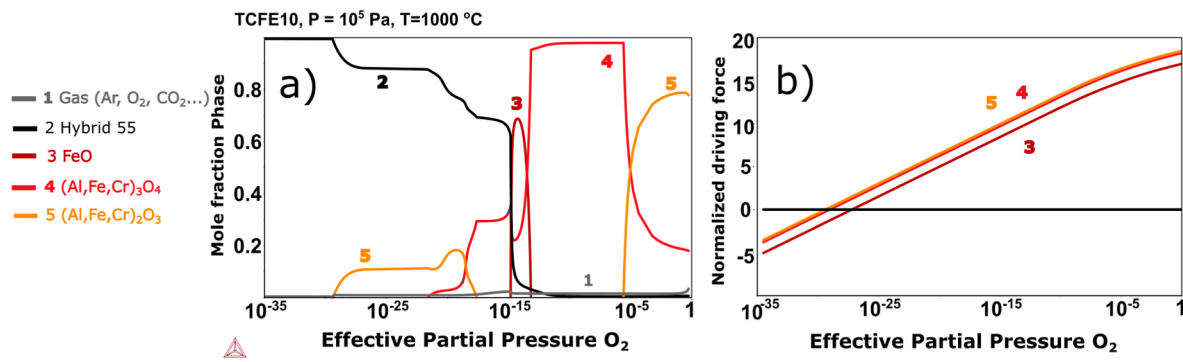


Fig. 3. a) show which oxides may form in the cutting zone due to oxidation of the workpiece, it is the equilibrium phase fractions when Hybrid 55 reacts with oxygen as a function of the effective partial pressure of O₂ b) The driving force for these phases to form dependent on the effective partial pressure of O₂. This show which phases are more likely to form. The corundum phase (Al,Fe,Cr)₂O₃ and spinel phase (Al,Fe,Cr)₃O₄ have a higher driving force than FeO.

oxide is stable at low effective partial pressures (below 10⁻¹⁷) and high partial pressures (above 10⁻⁶). (Al,Fe,Cr)₂O₃ has the highest driving force for formation, while FeO is only stable in the range of 10⁻¹⁵-10⁻¹³ and has the lowest driving force of formation. (Al,Fe,Cr)₃O₄ spinel phase is stable above a partial pressure of 10⁻²⁰ and has a driving force close to (Al,Fe,Cr)₂O₃ (Fig. 3a). The steel can also dissolve a small amount of oxygen before an oxide forms (Fig. 3a). These general trends are robust for temperatures from 25 °C and up to 1200 °C and for pressures from 10⁵ Pa up to 10⁹ Pa.

(Al,Fe,Cr)₂O₃ and (Al,Fe,Cr)₃O₄ are both stable at high and low O₂ partial pressures (Fig. 3a) and have a high driving force for formation (Fig. 3b). Thus, they are the most likely to form and remain stable. FeO on the other hand is stable in a narrow range of effective oxygen partial pressures and has a lower driving force for formation than the other two reaction products (Fig. 3a). Modeling was also performed for a hypothetical steel that do not contain aluminum and chromium, these show a reverse trend dominated by the formation of FeO.

Oxides such as aluminum oxide, can act as a barrier to oxidative tool wear of multilayer CVD coated cemented carbide tool [22].

However, FeO can react with a cBN tool and cause tool degradation [27]. Hence, both positive and negative effects are expected from the formation of workpiece oxides on tool surfaces. It can protect against oxidation or catalyze the oxidation. The effect depends on the interaction between the formed product and the tool material, determined by cutting process interactions (*interaction iv*).

3.2. Oxidation of the tool material (ii)

The reaction between the tool and the environment can be modeled in the same way as the interaction between workpiece and environment. Hence, the section below relates to category *ii* *Oxidation of the tool*. This section aims to shed light on whether the tool degraded by oxidative wear mechanisms and under which conditions such wear processes take place.

3.2.1. Silicon-containing tools (Si₃N₄, Al₂O₃-SiC_w, SiAlON)

The silicon nitride (Si₃N₄) tool material is not thermodynamically stable (metastable) at ambient total gas pressures. Hence, the amount of

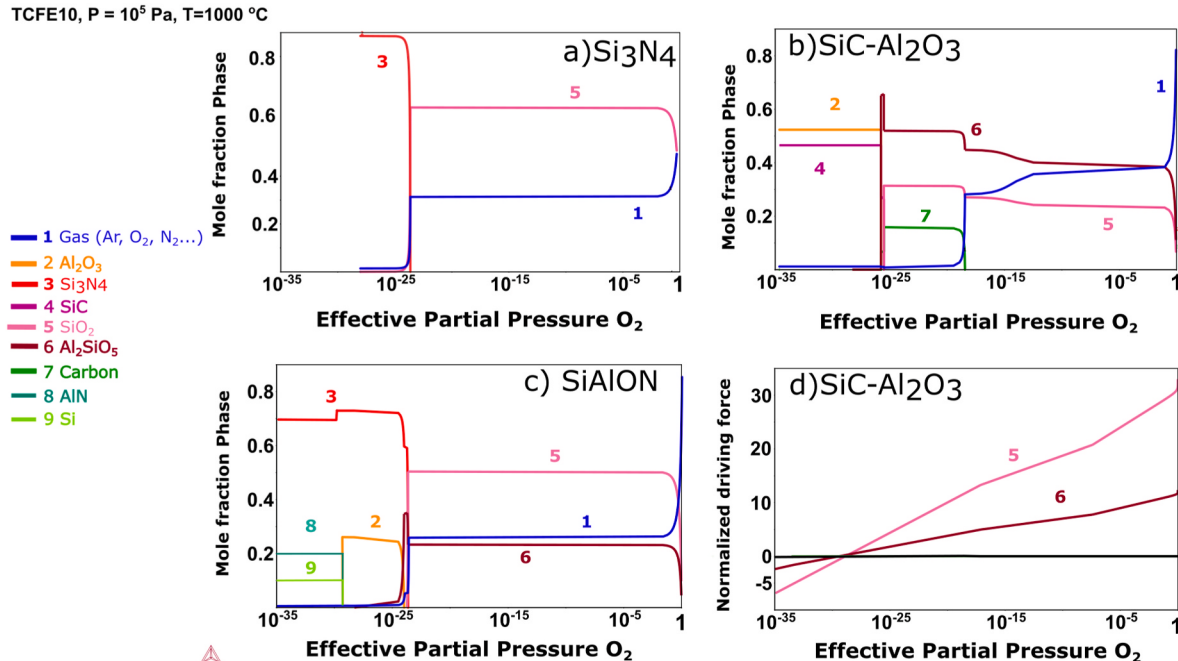


Fig. 4. a) Modeling results showing the oxidation of Si₃N₄, leading to formation of SiO₂ with increasing effective partial pressure of O₂ b) and c) showing similar calculation results for Al₂O₃-SiC_w and SiAlON tools, both reactions leading to the formation of Al₂SiO₅ in addition to SiO₂. d) The driving force for formation of SiO₂ and Al₂SiO₅ versus increasing oxygen availability in the representative case of the Al₂O₃-SiC_w tool.

Si_3N_4 decreases to zero at an effective O_2 partial pressure of 10^{-23} , as it decomposes to SiO_2 and gas as the effective partial pressure of O_2 increases, given a high enough temperature and time. This is seen in Fig. 4a where the molar phase fractions is plotted as function of increasing effective oxygen partial pressure. The trend remains unchanged within the range of cutting temperatures and pressures investigated in this study. However, calculations show that increasing the temperature increases the effective partial pressure at which SiO_2 becomes stable. Decreasing the pressure increases the effective O_2 partial pressure at which SiO_2 becomes stable. The behavior of $\text{Al}_2\text{O}_3\text{-SiC}_w$ is similar insofar as the trends are stable across cutting temperatures and pressures. However, $\text{Al}_2\text{O}_3\text{-SiC}_w$ degrades into SiO_2 , Al_2SiO_5 and graphite, as shown in Fig. 4b. This is followed by the oxidation of graphite and the formation of CO_2 gas at elevated temperatures.

Finally, SiAlON is a more complicated phase to model, since it basically inherits the lattice structure of Si_3N_4 but with partial replacement of Si–N bonds by Al–O and Al–N bonds [38]. Fig. 4c show that Al_2SiO_5 , SiO_2 and gas phases are the most stable as the effective partial pressure of O_2 increases. Thus, SiAlON resembles both Si_3N_4 and $\text{Al}_2\text{O}_3\text{-SiC}_w$ decomposition. Fig. 4d show the driving force for the formation of SiO_2 and Al_2SiO_5 versus an increasing effective partial pressure of O_2 in the case of $\text{Al}_2\text{O}_3\text{-SiC}_w$. The trend is the same for all three silicon-containing tools since the carbon present in SiC transform into graphite and CO_2 and excess nitrogen transform into a gas when thermodynamic equilibrium is reached.

Silicon-containing tools have different mechanical properties [39] but are predicted to degrade in an oxygen environment in a similar manner (Fig. 4a–c). The silicon will react with the oxygen to form SiO_2 (Fig. 4). The presence of aluminum, as in the case of SiAlON and $\text{Al}_2\text{O}_3\text{-SiC}_w$, additionally results in the formation of Al_2SiO_5 (Fig. 4b–d). Neither of the elements C or N are likely to participate in the formation of protective reaction products (Fig. 4b and c). Both the predicted formation of SiO_2 and Al_2SiO_5 would lead to a rapid degradation of these tool materials [28].

3.2.2. Coated cemented carbide tools (WC-Co , $(\text{Ti},\text{Al})\text{N}$)

For the purpose of modeling, the cemented carbide tool with a PVD $(\text{Ti},\text{Al})\text{N}$ coating can be divided into the following four phases: two for the substrate WC and cobalt metal and two for the coating TiN and AlN . Such a representation of the $(\text{Ti},\text{Al})\text{N}$ coating is related to the fact that $(\text{Ti},\text{Al})\text{N}$ is a metastable phase at the modeled conditions. Although modeled, WC and cobalt phases are not shown in Fig. 5 for reasons of clarity. The substrate is known to oxidize and the focus of the study is the coating. The wear rate of cemented carbide is also more rapid and more studied than $(\text{Ti},\text{Al})\text{N}$ [34,35]. Fig. 5a shows the equilibrium phase fractions for TiN and AlN , versus an increased effective partial pressure of O_2 . $(\text{Ti},\text{Al})\text{N}$ will degrade into TiO_2 and $(\text{Al},\text{Ti})_2\text{O}_3$ while nitrogen will form N_2 . Fig. 5b shows that the driving force for the formation of TiO_2 and $(\text{Al},\text{Ti})_2\text{O}_3$ is steadily increasing with an increasing availability of

oxygen.

The coating will tend to oxidize but the rate of the oxidation will depend on the temperature in the cutting zone and the availability of oxygen (Fig. 5). Hence, the degradation of the coating by the formation of TiO_2 and $(\text{Al},\text{Ti})_2\text{O}_3$ is predicted to be the main oxidational wear mechanism for the $(\text{Ti},\text{Al})\text{N}$ coating (Fig. 5).

3.2.3. Titanium carbide-containing tools ($\text{Al}_2\text{O}_3\text{-TiC}$, cBN-TiC)

Fig. 6a gives the equilibrium phase fractions for the TiC phase present in the tool dependent on the effective partial pressure of O_2 . This calculation is valid for the oxidation of only the TiC binder in both $\text{Al}_2\text{O}_3\text{-TiC}$ and cBN-TiC tools. First, Ti_2O_3 forms at lower partial pressures and TiO_2 at higher partial pressures of O_2 and the carbon will form CO_2 gas (Fig. 6a). The driving force for the formation of TiO_2 and Ti_2O_3 , in turn, depends on the partial pressure of O_2 . The driving force for the formation of Ti_2O_3 is initially higher. Then driving force for formation of TiO_2 surpasses than of Ti_2O_3 at higher effective partial pressures (Fig. 6b). However the difference between TiO_2 and Ti_2O_3 is small (Fig. 6a). Al_2O_3 does not react with oxygen at any machining temperatures and pressures. Hence, the $\text{Al}_2\text{O}_3\text{-TiC}$ tool should only experience an oxidational attack on the TiC and not Al_2O_3 .

The TiC-cBN tool will not only experience oxidational attack on TiC but also on the BN phase. Hexagonal boron nitride is the equilibrium BN phase at these temperatures and pressures, since cubic-BN is metastable at these conditions. Oxygen reacts with BN to form B_2O_3 (Fig. 7), which has a melting temperature of approximately 450°C . Fig. 7 also shows that the driving force for the formation of B_2O_3 increases at higher effective O_2 partial pressure. The formation of B_2O_3 might potentially form a protective film on the tool surfaces, but such a product might melt or be abraded away during the cutting process. Calculations also show that increased pressures will increase the melting point of B_2O_3 without affecting other aspects of interaction.

3.3. Chemical and diffusional wear (iii) and the cutting process (iv)

Chemical and diffusional wear should be studied in addition to wear by oxidation, this is done by investigating whether the tool material is likely to react or dissolve into the workpiece material. In this section we also combine all three components of tool degradation: *oxidation of workpiece material (i)*, *oxidation of tool material (ii)* and *chemical and diffusional wear (iii)*. The calculations were also performed for temperatures from 25°C and up to 1200°C , for pressures from 10^5 Pa up to 10^9 Pa . This combination of mechanisms can predict whether the workpiece oxides or tool/workpiece reaction products could protect the tool from oxidation, diffusion and chemical wear or whether, on the contrary, if it will accelerate the degradation of the tool material. Technically, this can be performed in one single calculation because the workpiece material always has minor concentrations of dissolved oxygen, and an effective partial pressure of O_2 equaling zero is the same as a direct tool/

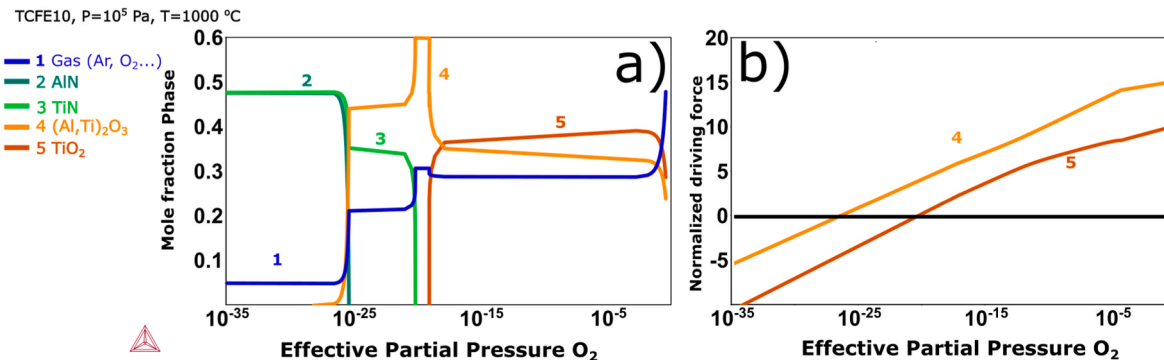


Fig. 5. a) Results from the equilibrium calculations between the modeled $(\text{Ti},\text{Al})\text{N}$ coating and oxygen. $(\text{Ti},\text{Al})\text{N}$ degrades into TiO_2 and $(\text{Al},\text{Ti})_2\text{O}_3$ together at increasing effective partial pressures of O_2 . b) Showing the driving force for the formation of TiO_2 and $(\text{Al},\text{Ti})_2\text{O}_3$.

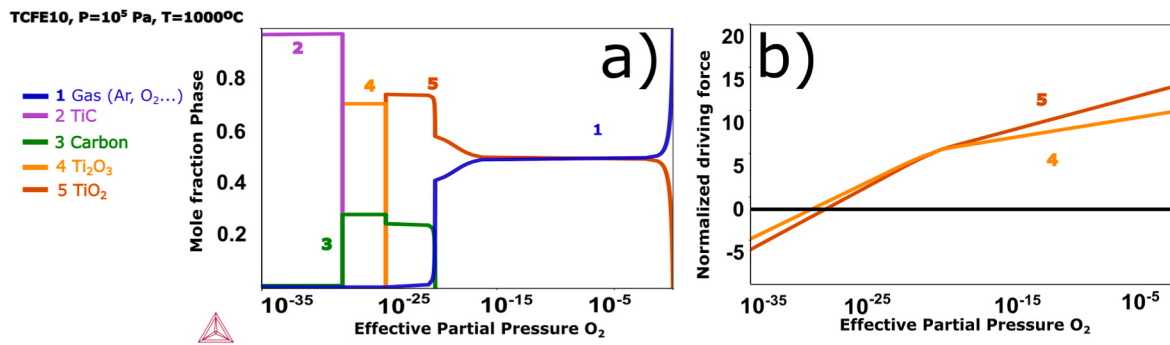


Fig. 6. a) The TiC present in both the Al_2O_3 and cBN tools can react with oxygen and form TiO_2 or Ti_2O_3 . b) The driving force for formation of TiO_2 and Ti_2O_3 . Ti_2O_3 has a higher driving force at a low effective O_2 partial pressure and TiO_2 at high effective O_2 partial pressures.

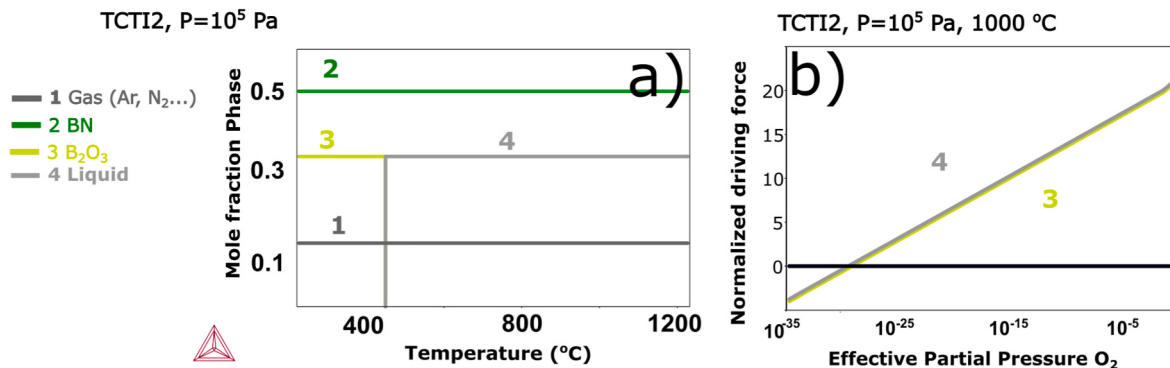


Fig. 7. Showing the molar phase fractions a) and driving force for formation b) for the interaction between BN and O_2 . The formation of B_2O_3 is a result of BN oxidation. Under static conditions, B_2O_3 acts as an oxidation barrier, yet it melts and lacks the mechanical properties to function under the thermo-mechanical loads of cutting.

workpiece interaction (iii). Hence this section models the combination of all the multi component interactions in cutting process (iv).

3.3.1. Silicon-containing tools (Si_3N_4 , $Al_2O_3-SiC_w$, $SiAlON$)

Silicon-containing tools are highly prone to oxidative wear according to earlier calculations given in Fig. 4. Fig. 8 gives the equilibrium phase composition of Hybrid Steel® 55 in contact with Si_3N_4 simultaneously under an increasing partial pressure of O_2 . The phases in the red zone of Fig. 8 show the interaction at low O_2 partial pressures, where no new oxides are stable. This red zone represents the interaction (iii)-chemical and diffusional wear between the steel (workpiece/chip) and Si_3N_4 . The region outside the red area represents the combined effect of (i), (ii) and (iii), the cutting process (iv).

Si_3N_4 is in a stable phase at low effective oxygen partial pressures (red zone). Nevertheless, some N has formed AlN and (V,Cr)N (Fig. 8), a chemical interaction has to occur for these nitrides to form. Si_3N_4 is a stoichiometric phase and no new Si phase is formed at these low effective oxygen partial pressures. This result indicates that the Si has dissolved in the steel. This dissolution of Si indicates the possibility for diffusional interactions. This might not be obvious from Fig. 8, however the calculation contains all the thermodynamic properties of the system (Section 2.1 and Appendix A). Fig. 9 give the mole fraction of phases as a function of small additions of Si_3N_4 to the system. Showing that the steel can dissolve all the Si in Si_3N_4 , up to an addition corresponding to the dotted line. It also shows the stability of the AlN and (V,Cr)N reaction products.

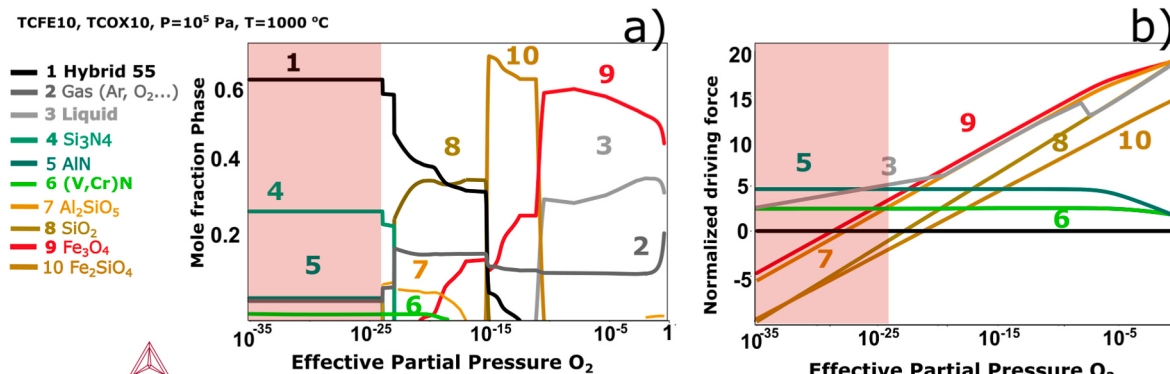


Figure 8. Showing the interactions (iii) and (iv) for the Si_3N_4 tool material. The products $(Al,Fe,Cr)_2O_3$, $(Al,Fe,Cr)_3O_4$ and SiO_2 in Figs. 3 and 4 are the results of the interaction (i) and (ii), which are now replaced by the reaction products Al_2SiO_5 and Fe_2SiO_4 . Because combining interaction (i), (ii) and (iii) results in combination effects, hence (iv)-the cutting process shown by the schematic in Fig. 1.

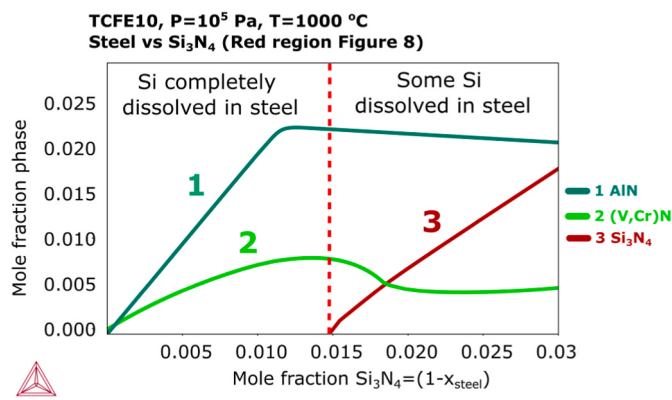


Fig. 9. Showing how Si can be completely dissolved in steel while N forms AlN and (V,Cr)N, indicating possible Si diffusion during machining.

SiO_2 , Al_2SiO_4 and Fe_2SiO_4 become stable at even higher effective O_2 partial pressures (Fig. 8). However, Fe_2O_3 and a liquid phase containing silicon, metals and oxygen are both more thermodynamically favorable when the effective O_2 partial pressure is approximately 10^{-10} or above. The calculations predict that the mole fraction of products will differ for the $\text{Al}_2\text{O}_3\text{-SiC}_w$ and SiALON tools. However, the reaction products and their behavioral trend are similar since both carbon and aluminum are already present in the steel (Fig. 8).

Silicon-containing tools, as exemplified in the case of Si_3N_4 , are likely to degrade by oxidation wear by the formation of SiO_2 and N_2 (Fig. 8). Additionally, Si tends to dissolve in the workpiece material (Fig. 9). Furthermore, Si will also react with any of the metal oxides from the workpiece oxidation (Fig. 3), thereby forming glassy phases such as Al_2SiO_5 and Fe_2SiO_4 (Fig. 8). Another possible and positive scenario might occur if the nitrogen reacts with the steel alloys Al, V and Cr, thereby forming nitrides instead of becoming gaseous N_2 . The formation of such nitrides on the interface might retard tool degradation, however it might lead to abrasion if formed as particles. The iron-rich spinel Fe_3O_4 has a slightly higher driving force than the other phases in the predictions (Fig. 8) and this stable phase might protect the tool by acting as a barrier for further oxidation or diffusional dissolution. However, Si from the tool can react with this spinel and form Fe_2SiO_4 (Fig. 8), which would decrease its ability to protect the tool as it melts slightly above 1100 °C [40]. Fe, Ni and Cr can diffuse into the whiskers while Si diffuses out or oxidizes [41]. However, this would not lead to the formation of any tool protective layer. Changing the pressure and temperature does not significantly change the above interactions, but rather shifts the point at which the phases forming under high effective O_2 partial pressure become thermodynamically favorable.

3.3.2. Coated cemented carbide tool (WC-Co , $(\text{Ti},\text{Al})\text{N}$)

Oxidation can be significant in the case of the $(\text{Ti},\text{Al})\text{N}$ coating as

reported earlier in Fig. 5. The calculation results for the interaction with the addition of Hybrid Steel® 55 steel are shown in Fig. 10. Previously, the excess nitrogen released due to oxidation of $(\text{Ti},\text{Al})\text{N}$ can now promote the formation of refractory nitride $(\text{V},\text{Cr})\text{N}$ (Fig. 10), similar to the results in (Fig. 8). However, the oxidation of the coating remains the most significant interaction. The driving force for the formation of $(\text{Al},\text{Ti},\text{Fe})_2\text{O}_3$ and $(\text{Al},\text{Fe})_3\text{O}_4$ still remains the largest and both phases are stable under high partial pressures of O_2 .

Corundum $(\text{Al},\text{Ti},\text{Fe})_2\text{O}_3$ and spinel $(\text{Fe},\text{Al})_3\text{O}_4$ (Fig. 10) are more capable of protecting the coating from oxidation than the oxides containing silicon (Fig. 8), as these interaction products are not glassy phases. The calculations also predict that the solubility of Ti, Al and N in steel is less than of Si. The metal oxides that form between the tool and the workpiece (Fig. 10) might also limit further oxidation and dissolution of the tool (Figs. 5 and 10).

3.3.3. Titanium carbide-containing tools ($\text{Al}_2\text{O}_3\text{-TiC}$, cBN-TiC)

Titanium carbide can degrade due to oxidation by transforming into Ti_2O_3 and TiO_2 , as shown in Fig. 5. Alumina does not oxidize, while cBN will oxidize with a release of N_2 gas and the formation of B_2O_3 , which becomes liquid above 450 °C at 10^5 Pa (Fig. 5). The calculation results in Fig. 11 show that the alumina phase with different compositions of $(\text{Al},\text{Fe},\text{Cr})_2\text{O}_3$ is stable (Fig. 11a) and has a high driving force for formation. $(\text{Al},\text{Fe},\text{Cr})_3\text{O}_4$ spinel is also thermodynamically stable and has virtually the same high driving force. Fig. 11 illustrate that $\text{Al}_2\text{O}_3\text{-TiC}$ tool material will degrade through oxidation of TiC followed by the formation of Ti_2O_3 and the simultaneous dissolution of carbon in the steel. However, the dissolution of TiC is less favorable than its oxidation. Boron and nitrogen can also dissolve in the workpiece and chips similar to Si (Figs. 8 and 9), thus fulfills the criteria for diffusional wear and they can react and form borides and nitrides leading to chemical wear (Fig. 11).

The predictions also reveal that the cBN-TiC material is less resistant to chemical, oxidation and diffusional wear compared to the $\text{Al}_2\text{O}_3\text{-TiC}$ material (Fig. 11). Both materials share the same TiC component but Al_2O_3 is essentially inert while cBN has many possible degradation paths. The calculation predict that the ratio of metallic elements in the spinel phases $(\text{Al},\text{Fe},\text{Cr})_3\text{O}_4$ and corundum phases $(\text{Al},\text{Fe},\text{Cr})_2\text{O}_3$ will be determined by the effective oxygen partial pressure. Starting from Al and Ti based oxides and shifting towards Fe and Cr. The formation of all such phases would have the possibility to form a TPL and slow down the tool degradation (Figs. 6, 7 and 11).

4. Experimental validation

The results from the cutting tests and microscopy are given in this section, it is divided in 3 parts as the previous Section 3 thus 1. Silicon-containing tools (Si_3N_4 , $\text{Al}_2\text{O}_3\text{-SiC}_w$, SiALON), 2. Coated cemented carbide tools (WC-Co , $(\text{Ti},\text{Al})\text{N}$) and 3. Titanium carbide-containing tools ($\text{Al}_2\text{O}_3\text{-TiC}$, cBN-TiC). The tool life criteria is set to $\text{VB} = 200 \mu\text{m}$ and

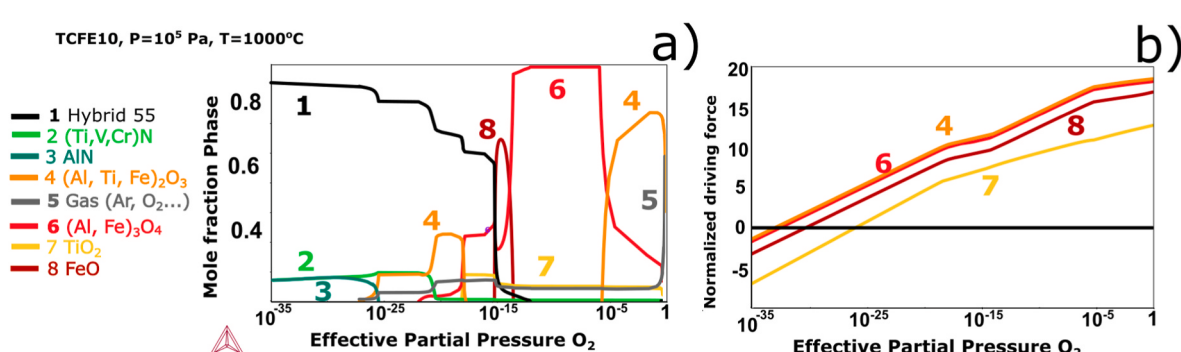


Fig. 10. The equilibrium calculation and driving force calculation for the interaction products forming due to interactions between the $(\text{Ti},\text{Al})\text{N}$ -coated carbide tool, the steel and oxygen. The reactions between Fe-Al-Ti-O are the most prominent reaction products that might hamper further oxidation of the tool material.

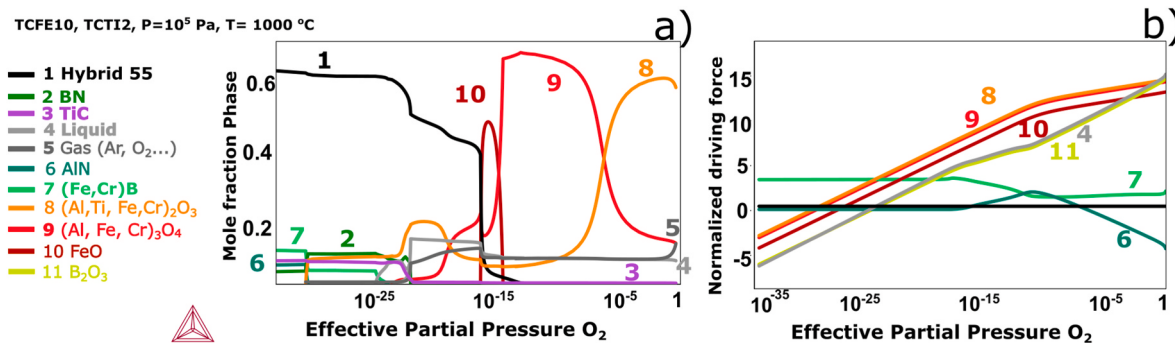


Fig. 11. a) The phase fractions for cBN with TiC binder and Hybrid steel 55 as a function of increasing effective partial pressure of oxygen, and, b) corresponding driving force for the formation of the reaction products.

$KT = 30$ (Section 2.2).

4.1. Silicon-containing tools (Si_3N_4 , $Al_2O_3-SiC_w$, $SiAlON$)

Fig. 12 shows the development of flank wear and crater wear for silicon-containing tools versus engagement time. The Si_3N_4 tool displayed the shortest tool life of around 30 s and the process was stopped due to excessive cratering. The $Al_2O_3-SiC_w$ had a tool life of 75 s and failed due to crater wear. The $SiAlON$ tool had the longest tool life, lasting for 200 s then reached the crater wear criteria. Such excessive cratering behavior is indicative of chemical and diffusional degradation [34,35]. The $SiAlON$ tool developed the largest degree of flank wear, which points to a concurrent abrasive wear mechanism, whereas the short tool life of $Al_2O_3-SiC_w$ and Si_3N_4 tools did only allow for small amounts of flank wear to develop (Fig. 12).

Fig. 13 show BSE-SEM images and XEDS spectra of the worn $SiC-Al_2O_3$ tool taken of the ejection, sliding and sticking zones of the cutting edge after 90 s of machining. This is representative of the main wear mechanism of the Si-based tools. In addition BSE-SEM images and a spectra of the unworn tool material, was also collected and compared to the different regions of the cutting zones. The spectra are acquired from an area scan and also a point analysis of a whisker from the respective wear zones. This kind of comparative analysis is performed for a) the new tool and the different zones of a worn tool (after 75 s of machining) - b) the debris ejection zone, c) sliding zone and d) sticking zone.

The ejection zone b) is located outside the tool/chip interface and has high concentrations of Mg, O, Fe, Ca, Cr and Mn indicating that this is oxidized workpiece material deposited outside the cutting zone (Fig. 13, surface spectra b). The SiC whiskers are not detectable through this thick layer of metal and oxides.

For the sliding zone c), high concentration of Fe, Cr, Ni, Ca and O on the tool surface and a significant decrease of Si and loss of C is detected (Fig. 13, surface spectra c). The BSE image reveals the presence of a thin film across the entire surface of the sliding zone. A spectrum from the

remnants of the whiskers in this area (Fig. 13, whisker spectra c) shows a critical loss of Si, which is replaced by Fe, Ni, V, Cr and Mn, indicating a counter-diffusion of elements. This indicates a preferential degradation of the whiskers in this contact region.

Within the sticking zone d) a smaller loss of Si and a greater loss of C is observed, if compared to the sliding zone c). Additionally, XEDS also indicate the presence of Fe, Ni, V, Cr and Mn, similarly to the sliding zone. Yet the former whisker region is practically devoid of Si in the sliding zone c), while some Si is present in the whiskers in the sticking zone d) (Fig. 13: whisker spectra c and d).

Comparing and combining the results from machining and modeling show that the Si from the whisker can react with oxygen and steel to form SiO_2 , Al_2SiO_5 , Fe_2SiO_4 due to the high driving forces of these phases, predicted by the calculations shown in Fig. 8 and Section 3.3.1. Which is due to oxygen generally being available in the sliding zone c). Thus, this kind of reaction lead to the depletion of Si from the whiskers, shown by the smaller Si peak in whisker spectrum c in Fig. 13. This is in agreement with loss of the SiC phase in Fig. 4b. The BSE-SEM image of the sliding zone shown by a glassy appearance which is in agreement with the calculation of the formation of a of Al_2SiO_5 , Fe_2SiO_4 (Fig. 8), shown by the Fe, Al, Si and O peaks in surface spectra c in Fig. 13. This is also in agreement with other studies of Si-tools [41]. Additionally, the Si and C peaks are replaced by with workpiece elements peaks in the whisker spectra d) Fig. 13 which reflects a counter-diffusional process of Si and workpiece metals in agreement with [42] and predictions in Figs. 8 and 9. Thus, diffusional and oxidation wear is present in the sliding zone, in agreement with predictions Section 3.3.1. Oxidation is suppressed and only the diffusional loss of silicon (Section 3.3.1) is active [28], due to the limited oxygen availability in the sticking zone d). This leads to the replacement of silicon by Fe, Ni, Cr and V in the whisker (Fig. 13) and an absence of a glassy phase in this contact zone d).

4.2. Coated cemented carbide tool (WC-Co, (Ti,Al)N)

The coated cemented carbide tool initially displayed limited crater

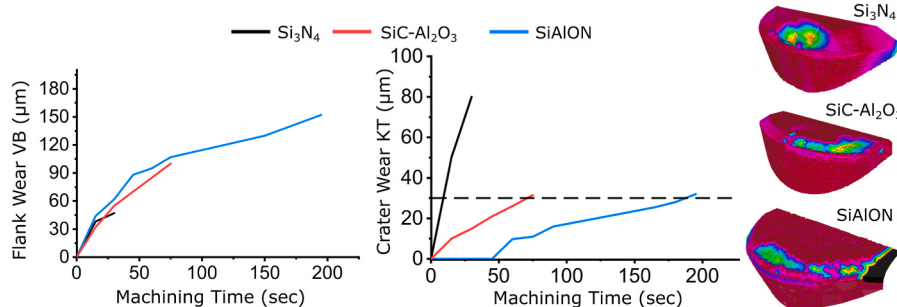


Fig. 12. Tool wear evolution of silicon-based tools and 3D scans of the worn tools.

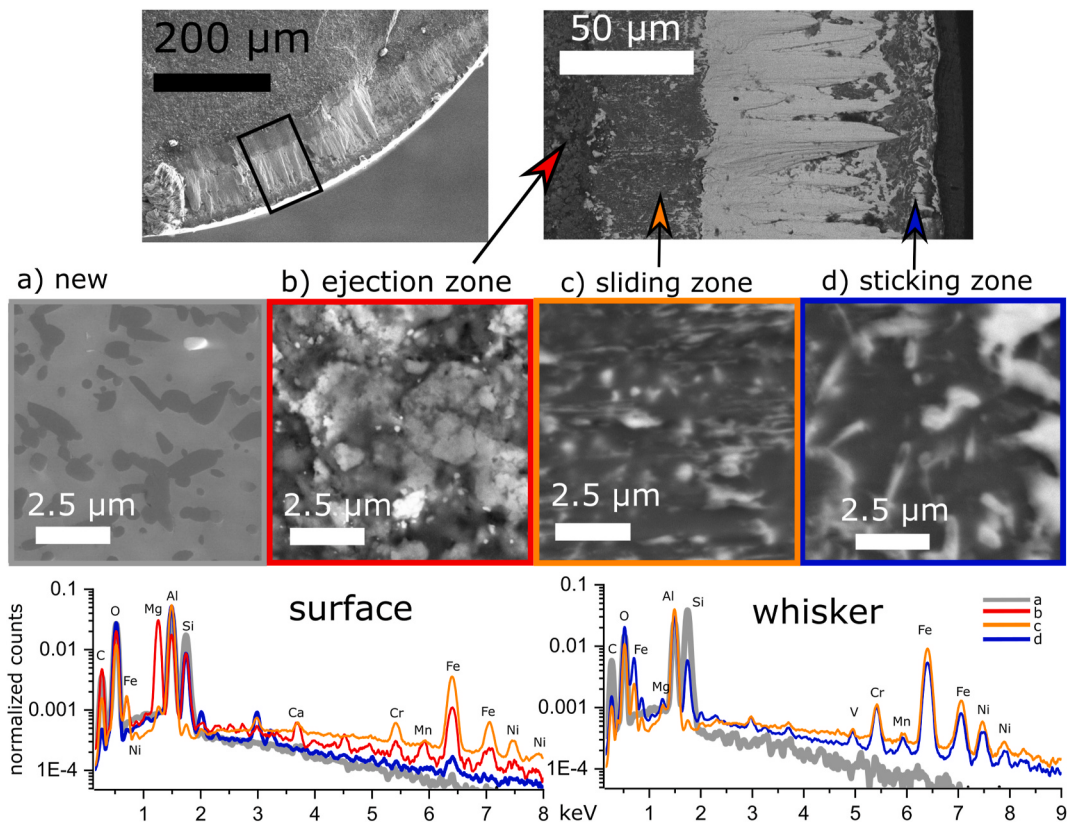


Fig. 13. BSE-SEM images and the tool and cutting zone after 90 s of machining with the SiC-Al₂O₃ tool. Additional BSE-SEM image of the unworn tool material compared to the different regions of the cutting zone. The XEDS spectra are collected and compared, one type of spectra are collected from the whole surface and one from point measurements of the whiskers.

wear and flank wear (Fig. 14). The crater wear was absent until 150 s of machining which was followed by flank wear. This rapid growth of wear resulted in plastic deformation of the cutting edge.

Fig. 15 shows a topography-sensitive SE image, a composition-sensitive BSE image and XEDS spectra of the rake of the tool after 90 s in cut. Three coating perforations or pits are filled with workpiece material, as indicated by the yellow arrows Fig. 15. The growth and coalescence of such pits led to the sudden large increase in rake wear (Fig. 14). Two distinct surface morphologies can be seen in the contact zone, as compared to the original coating spectrum a) Fig. 15. The first area of interest spectrum b) reflects the adhered workpiece material and area/spectrum c) has a visible thin film. In the BSE image, the thin film c) is brighter than the original coating a), but not the ahead metal b), due to the Z-contrast mechanism. As expected, the adhered metal b) mainly comprises of Fe, C, Cr and Ni. However, since the thickness of the adhered metal film is less than the XEDS interaction volume Ti and N

from underlying coating, are also detected. The area within the detected film c) shows a strong signal of Al, Fe and O but is depleted of Ti, compared to the original coating.

Linking the results from calculations and machining can explain how the (Ti,Al)N coated tool had a tool life comparable to the SiAlON tool and longer than the Si₃N₄ and Al₂O₃-SiC_W. Such a favorable performance is likely related to the more limited solubility of Ti and Al in the steel compared to Si (Section 3) rather than the addition of the chip breaker. A chip breaker changes the cutting conditions, but no the general thermodynamic trends. Additionally, the coating is more resistant to oxidation due to a smaller driving force for formation of reaction products than then the Si tools (Figs. 8 and 10). However, the formation of the film (Fig. 15) on top of the coating in the contact length play a larger role. The glassy film in Fig. 13 allowed Si to leave the whiskers while the film in Fig. 15 protect the coting. The expected reaction products (Fig. 10) point to the formation of (Al,Fe)₂O₃ and (Al,Fe)₃O₄,

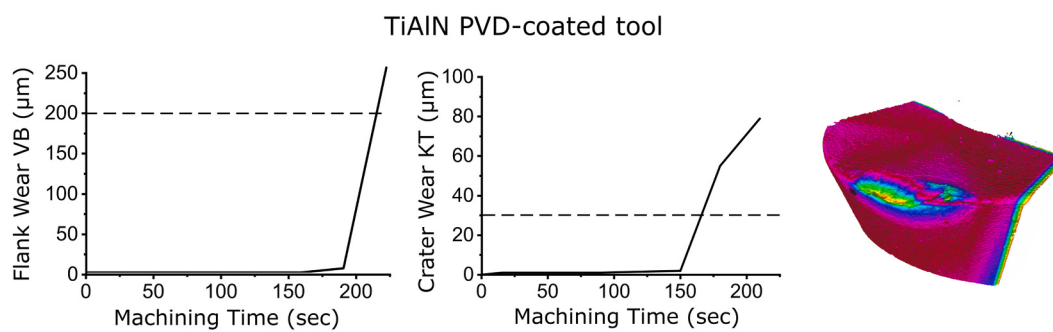


Fig. 14. Evolution of flank and crater wear of PVD (Ti,Al)N-coated cemented carbide, showing limited wear progression then a sudden increase after 150 s. The rapid increase in crater wear after 150 s led to the collapse of the cutting edge.

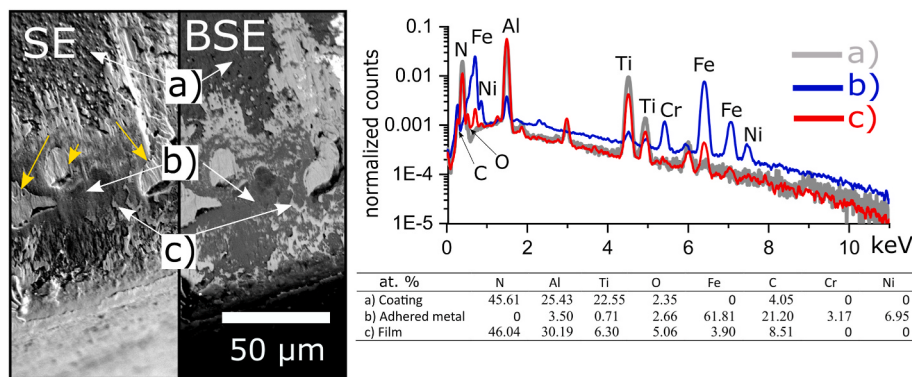


Fig. 15. SE and BSE images of the rake face of the (Ti,Al)N coated tool after 90 s of machining. Comparison of XEDS spectra and corresponding calculated compositions between the original coating a), adhered metal b) and film c). Yellow arrows indicating pits. (For interpretation of the references to colour in this figure legend, the reader is referred to the Web version of this article.)

which form *in operando* during the machining process. The regenerative and continuous formation of such a protective film on the tool surfaces that comprises of stable oxide phases would then explain the longer tool life [21], whereas for Si-containing tools, similar *in-operando* interaction leads to the formation of non-protective glassy phases [28].

4.3. Titanium carbide-containing tools (Al_2O_3 -TiC, cBN-TiC)

The cBN-TiC tool outperforms the Al_2O_3 -TiC tool with regard to resistance to flank wear (Fig. 16), which is explained by the differences in mechanical properties between the two materials [34,35]. However, cBN is expected to degrade from intensive chemical, diffusional and oxidative wear, while Al_2O_3 is affected by none of these, as shown in Section 3.2.3 and 3.3.3. Despite such expectations, crater wear for the cBN-TiC tool was less than for the mixed alumina tool (Fig. 16). Additionally, the progression of crater wear for the cBN-TiC tool significantly slowed down after 300 s (Fig. 16).

This kind of crater wear behavior is contrary to the classical relationship between solubility and driving forces and tool wear [12]. However, the formation of an $(\text{Al}, \text{Ti}, \text{Fe}, \text{Cr})_2\text{O}_3$ or $\text{Al}, \text{Fe}, \text{Cr}_3\text{O}_4$ (Fig. 11 and Section 3.3.3) tool protection layer might potentially explain this anomalous behavior [16]. Electron microscopy and spectroscopy (Fig. 17) show that a metal oxide film has formed on the contact surface of the cBN tool, similar to the film on the (Ti,Al)N-coated tool (Fig. 15). The thickness of such film can be approximated to several hundred nanometers based on the excitation volume of the SEM [43]. It is transparent at an accelerating voltage of 15 kV and visible at 5 kV (Fig. 17). XEDS confirms the presence of Fe, Cr, Al and O within this region. However, conclusive detection of Al and O is not possible as the tool material also contains Al_2O_3 , since it is used as a sintering aid for PcbN manufacturing [44], thereby affecting the baseline of the Al and O signal.

5. Oxidation and temperature investigation

Further investigation of the Al, Fe, Cr thin film (Figs. 15 and 17) and its dependence on cutting speed and oxygen availability is of considerable interest because predictive modeling show that this effect is driven by oxygen availability (Figs. 10 and 11) and its rate depends on the process temperature. The presence of high amounts of Al in the (Ti,Al)N-coated tool and the Al_2O_3 -TiC mixed ceramic makes the analysis of Al-based TPLs difficult. Hence, the investigation reported in this section will focus on cBN-TiC due to the observed stable TPL and low amount of Al present in the tool material. Thus enabling a clearer distinction to be made between parental tool material and a tool protection layer.

5.1. Method

The formation of reaction products and TPLs is a thermodynamic and kinetic process (Fig. 1). Thus, the temperature and chemical potential of the elements in the system will be determine the rate of TPL formation. Temperature measurements were conducted using a high-speed Flir x6580sc IR camera with an imaging frequency of 350 FPS (Hz) and a temperature range of 300–1150 °C. Orthogonal cutting was carried out rather than longitudinal cutting to enable correct imaging. Repeated orthogonal cutting experiments were performed with cutting speeds in the range of $v_c = 50$ –300 m/min and a feed rate $f = 0.1$ mm/rev using the same CBN010 insert material, but in a grooving geometry (LCGN160304-0300S0125LF) the width of cut equaling the tool geometry (3 mm). The implemented orthogonal cutting of the preliminarily prepared groove side and the camera-moving system enabled the measurement of the temperature field on the insert side view. The selected emissivity level was 0.55 for PcbN [45]. The temperature values were extracted from the image zone corresponding to the cBN-TiC part of the tool/chip contact zone (Fig. 18).

The investigation of the influence of oxygen was carried out by comparing an oxygen-reduced environment, ambient conditions and the

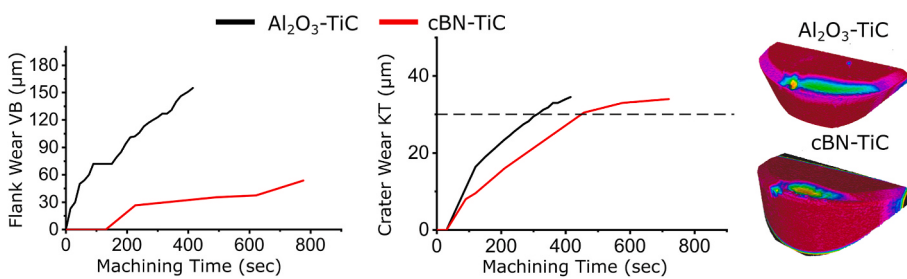


Fig. 16. Evolution of flank and crater wear for Al_2O_3 -TiC and cBN-TiC tools. The PcbN tool shows better resistance to flank wear, as expected from its mechanical properties. High resistance to crater wear was observed, while the tool material is expected to be less resistant to chemical wear.

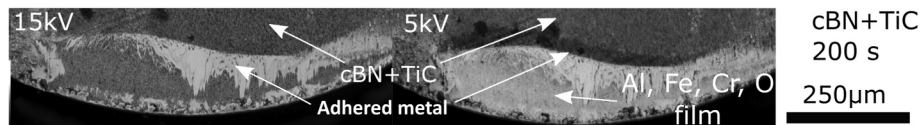


Fig. 17. Side-by-side BSE-SEM images of the rake of a cBN-TiC tool. A thin film of Al, Fe, Cr and O was detected when reducing the accelerating voltage (HV) to 5 kV.

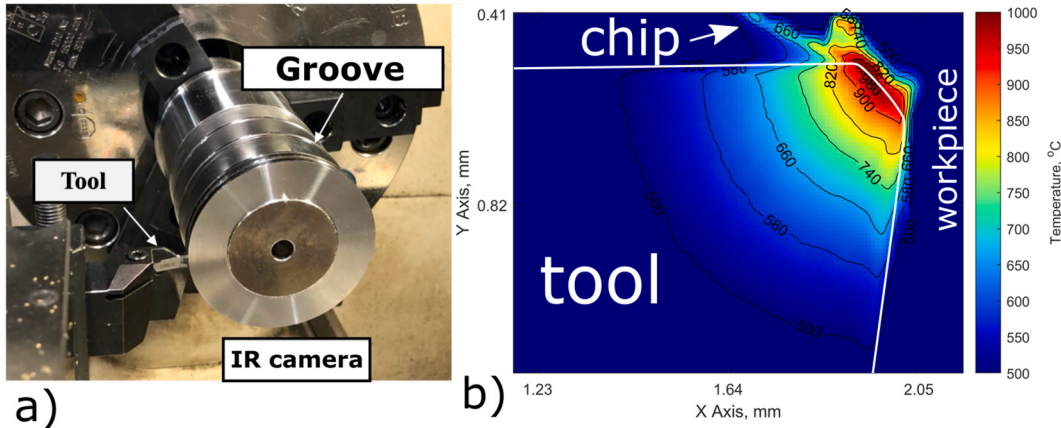


Fig. 18. a) The setup of the temperature measurements using an IR camera. The IR camera is out of view and filming orthogonal to the grooving. (b) A processed frame of a temperature field acquired for the orthogonal turning using CBN010 at $v_c = 300$ m/min and $f = 0.1$ mm/rev.

use of coolant. To perform such a comparison a special chamber was developed and used to control the availability of oxygen (Fig. 19). The chamber comprises a sheet metal frame covering the tool holder and partly the workpiece, it also contains internal tubing for gas supply. The chamber was subsequently purged with argon or compressed air to control the availability of oxygen. The gas was supplied through the chamber itself and through the tool holder having two rake and one flank jet nozzle. Argon gas supply at the flow rate of 400 l/m, which creates an essentially oxygen-free environment [21].

5.2. Results and discussion of oxidation and temperature investigation

As expected, the temperature in the cutting zone increases with increased cutting speed (Fig. 20) [46]. However, the temperature stabilizes at a cutting speed of $v_c = 200$ m/min (Fig. 20). Scanning electron microscopy at a low acceleration voltage of 5 kV was performed on tools after they have been used in the orthogonal temperature measurement tests. The BSE-SEM images in Fig. 20 give that there was no formation of a tool protection layer at low temperatures and speeds $v_c = 50$ –100 m/min. However a thin film identical to the TPL in Fig. 17, forms on the chamfer at speeds above 150 m/min. Thus, the TPL increases in thickness and coverage with increased speed and temperature. However, the rate at which the TPL is removed also increases, leading to its continuous

build-up and removal. Thus, the layer does not grow much beyond several hundred nanometers (Fig. 20). The formation and stabilization of the TPL with increased temperature limits the otherwise expected rapid tool wear because it acts as a barrier to further degradation [13].

Fig. 21 shows how the oxygen availability and the environment influence the performance and degradation of the respective tools. The machining in an oxygen-reduced environment was interrupted after 30 s due to severe vibrations, surface damage and chipping of the tool. Further SEM show that such anomalous process behavior was due to the strong adhesion of the chip to the tool, resulting in fractures on both the tool rake and flank. Also anomalous compared to machining in air, the use of a coolant had a negligible effect on both the flank and crater wear compared to the ambient conditions, despite the generally expected lowering of cutting temperature.

Comparing these results to previous calculations, show that such severe adhesion in an oxygen-reduced environment at a cutting speed of 300 m/min is likely due to the chemical and diffusional interaction between the steel and the cBN-TiC tool material, as seen in the calculation in Section 3.3.3 and Fig. 11. The potential formation of interfacial nitrides and borides could increase the strength of the adhesive bond, as known from the active brazing process [47]. The same calculation and Fig. 11 also show that $(\text{Al}, \text{Fe}, \text{Cr})_3\text{O}_4$ and $(\text{Al}, \text{Fe}, \text{Cr})_2\text{O}_3$ should form when there is more oxygen available, also seen in the SEM Fig. 17. This explains the longer tool life during machining in ambient and coolant conditions (Fig. 21). The benefit of using coolant instead of machining dry/ambient conditions is not significant for this combination of tool and workpiece at these cutting conditions, since the TPL is stable during dry conditions.

TEM lamellas were produced to further study the rake zone of the tools used in ambient and coolant conditions, this enabled an in-depth investigation of the film formed. The central image of Fig. 22 shows a Scanning Transmission Electron Microscopy (STEM) image of a lamella region with adhered metal on top and an interaction layer marked by red dashed lines on top of the cBN-TiC tool material. Selected Area Electron Diffraction (SAED) patterns were taken from the different areas indicated by the arrows, and XEDS-STEM line scans were made across the interaction layer shown at the bottom of Fig. 22.

The XEDS line scans indicate a decrease in Fe and Cr and an increase

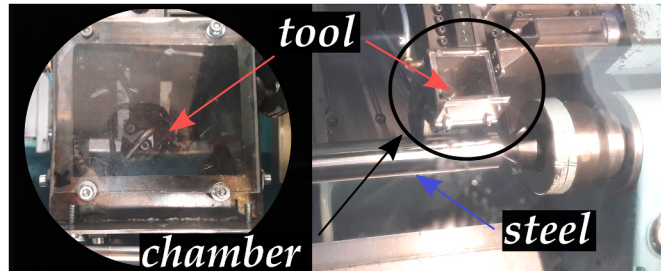


Fig. 19. Machining setup for cutting tests with limited oxygen in the cutting zone. Ar is supplied at a flow rate of 400 l/min from the jet nozzles in the tool holder and through the piping system in the chamber.

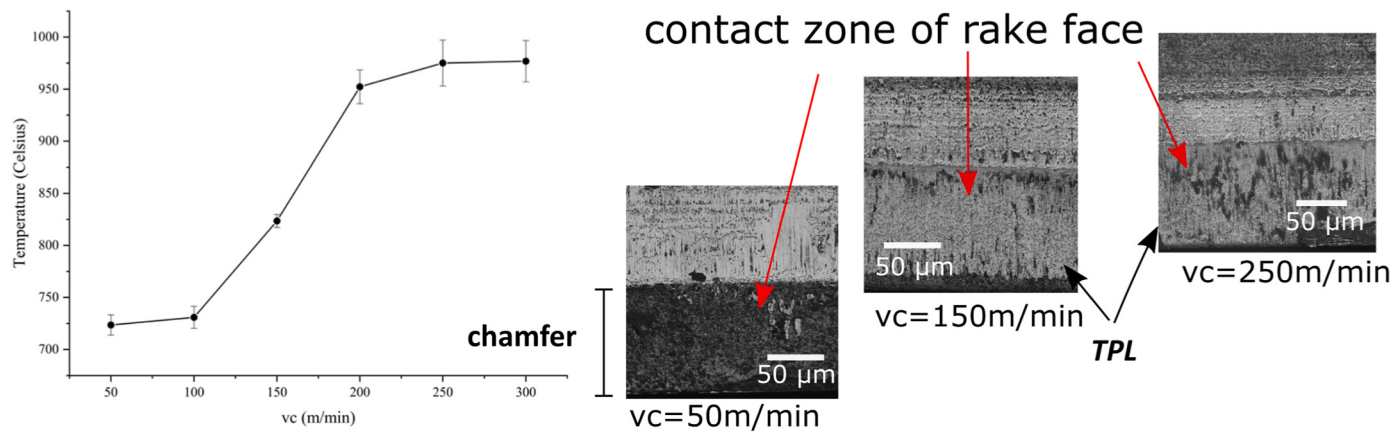


Fig. 20. Influence of cutting speed on process temperature for the cBN-TiC tool, with accompanying SEM-BSE images at surface-sensitive low acceleration voltages (HV = 5 kV), indicating the formation of TPL like the TPLs in Figs. 14 and 16.

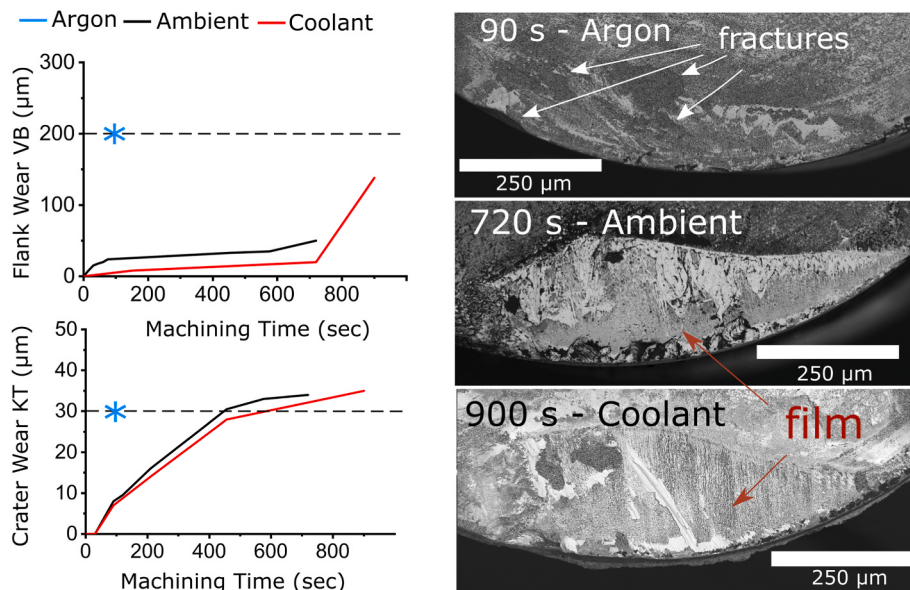


Fig. 21. Evolution of flank and crater wear for the cBN-TiC tools used in argon, ambient and coolant machining conditions. Accompanying low acceleration voltage (HV = 7 kV) BSE images showing the TPL in the case of ambient and coolant condition. Machining in an oxygen-reduced environment led to vibrations, adhesion, tool chipping and fractures.

in Al and O in the interaction zone. The B and N signals then increase at the edge of a cBN grain. The diffraction pattern from the adhered metal is consistent with iron in the bcc structure. Combining this information with XEDS-STEM indicates that it is adhered Hybrid Steel® 55 steel. The diffraction pattern from the interaction zone is not in agreement with any of the phases in the tool, binder, steel or FeO. The diffraction pattern is consistent with Al_2FeO_4 . However, conclusively ruling out Al_2O_3 was not possible. The observed Al_2FeO_4 is the same phase as the $(\text{Al}, \text{Fe})_3\text{O}_4$ predicted by the thermodynamic calculations. Thus, the thermodynamic predictions and the XEDS-STEM and XEDS-SEM analyses are all in agreement. Two lamella from different areas and tools were investigated using this combination of XEDS, SEM, TEM and SAED, and the investigation showed the same result. The observed Cr signal in the XEDS-STEM is in agreement with predicted solubility of Cr in the metal oxide phase. Thus, the formation of $(\text{Al}, \text{Fe}, \text{Cr})_3\text{O}_4$ takes place on the tool surface and between the tool and the adhered metal. The third diffraction pattern is from the tool just below the interaction layer showing the cubic structure of the cBN grain in the [1-1-2] direction.

6. Conclusions

Both the predictive modeling and the experiments showed that silicon-based ceramics tools suffered from degradation by reactions with the metal, atmospheric oxygen and metal oxides formed on the tool surface. The Si dissolved in the workpiece material by diffusion, it reacted with oxygen and workpiece metal oxides and formed glassy phases such as Al_2SiO_5 and Fe_2SiO_4 . Hence, reaction products formed on the tool surface *in-operando* are unable to retard the degradation of Si-based tools.

The predictive modeling indicated that machining Hybrid Steel® 55 with Al_2O_3 -TiC, (Ti,Al)-N-coated carbide and PcbN should lead to the formation of stable metal oxides of either Al_2O_3 or Al_2FeO_4 . Such oxides are expected to form a tool protection layer (TPL) that retards further tool degradation. Cutting tests, microscopy, spectroscopy and diffraction investigations confirmed the formation of $(\text{Al}, \text{Fe}, \text{Cr})_2\text{O}_4$ spinel predicted by the thermodynamic calculations, which slowed down the wear process. Additionally, machining in an oxygen-reduced environment and the temperature measurements showed that there is a minimum temperature and oxygen availability necessary for a stable TPL to

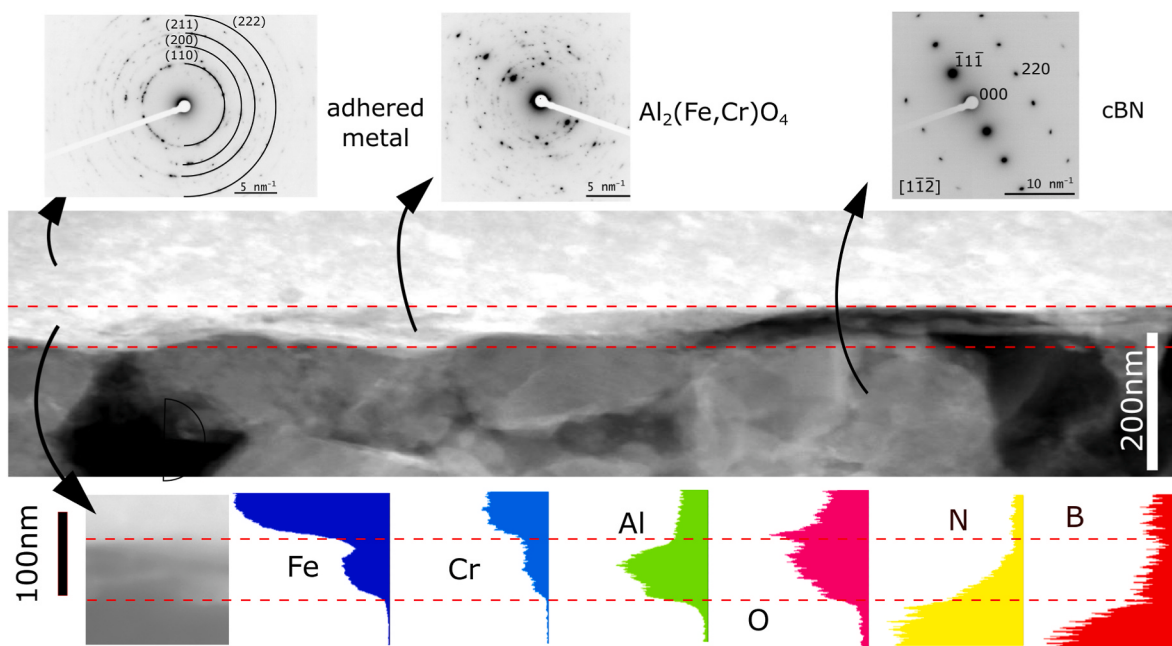


Fig. 22. SAED, combined with a STEM image and XEDS-STEM line scans showing the formation of an Al_2FeO_4 layer between the parental tool and the adhered workpiece metal. This film likely slows down further chemical, diffusional and oxidational wear.

form, in accordance with the modeling. Thus, a distinct improvement in tool wear resistance was demonstrated when the TPL formed, since it retarded otherwise expected chemical, diffusional and oxidational wear mechanisms.

Tool degradation during metal cutting due to chemical reactions, dissolution, diffusion and oxidation is well known. However, few models can make predictions about the result of these mechanisms when they occur concurrently and involve multi-component interaction systems, and no models found in literature have been able to predict the formation of tool protection layers. This study developed a thermodynamics-based modeling framework for prediction of such concurrent degradation mechanisms. Apart from tool degradation, the modeling was also constructed to enable prediction of *in-operando* formation of new phases which act as berries to tool wear. This framework was applied to the machining of Al-alloyed Hybrid Steel® 55 and 6 tool materials. Machining tests, microscopy, characterization of wear mechanisms and interaction products, control of machining environment and IR thermography constituted the experimental validation.

The developed modeling framework allows for the correct pairing of tool materials and workpiece alloying, leading to the formation of tool protection layers, before any machining is performed. Further modeling work, especially kinetic modeling enabling wear rate predictions, will benefit from using this method to predict what phenomena will influence the tool life. Since current kinetic models are not able to model all phenomena simultaneously. This framework also allows for combining and building on mechanical wear based models. Furthermore, the proposed modeling approach can predict what modification to the workpiece and tool composition will promote the formation of oxide, nitride, carbide or boride tool protection layer. Since it can predict the *in-operando* reactions occurring between the tool, workpiece and cutting environment.

CRediT authorship contribution statement

Axel Bjerke: Conceptualization, Methodology, Software, Validation, Formal analysis, Investigation, Data curation, Writing – original draft, Writing – review & editing, Visualization. **Andrii Hrechuk:** Conceptualization, Methodology, Validation, Formal analysis, Investigation, Data curation, Writing – original draft, Writing – review & editing,

Visualization. **Filip Lenrick:** Conceptualization, Methodology, Validation, Formal analysis, Investigation, Data curation, Writing – review & editing, Visualization, Supervision, Funding acquisition. **Andreas Markström:** Conceptualization, Methodology, Software, Validation, Formal analysis, Investigation, Resources, Writing – review & editing, Supervision, Funding acquisition. **Henrik Larsson:** Conceptualization, Methodology, Software, Validation, Formal analysis, Investigation, Resources, Writing – review & editing, Supervision, Funding acquisition. **Susanne Norgren:** Conceptualization, Methodology, Software, Validation, Formal analysis, Investigation, Resources, Writing – review & editing, Supervision, Funding acquisition. **Rachid M'Saoubi:** Conceptualization, Methodology, Validation, Resources, Writing – review & editing, Supervision, Funding acquisition. **Thomas Björk:** Conceptualization, Methodology, Validation, Resources, Writing – review & editing, Supervision, Funding acquisition. **Volodymyr Bushlya:** Conceptualization, Methodology, Validation, Formal analysis, Investigation, Resources, Data curation, Writing – review & editing, Visualization, Supervision, Project administration, Funding acquisition.

Declaration of competing interest

The authors declare that they have no known competing financial interests or personal relationships that could have appeared to influence the work reported in this paper.

Acknowledgements

This work was funded by the national strategic innovation program – national action for Metallic Materials, organized by Vinnova and Jernkontoret (Sweden) under the DEMO project (ID 2017-02915). The authors would like to acknowledge the Sustainable Production Initiative (SPI) – a cooperation between Lund University and Chalmers University of Technology. This acknowledgment also extends to Per Alm and Vyacheslav Kryzhanivskyy (Seco Tools AB) for their help with IR thermography.

Appendix A. Supplementary data

Supplementary data to this article can be found online at <https://doi.org/10.1016/j.wear.2021.203991>.

[org/10.1016/j.wear.2021.203991](https://doi.org/10.1016/j.wear.2021.203991).

References

- [1] C.A. van Luttervelt, T.H.C. Childs, I.S. Jawahir, F. Klocke, P.K. Venuvinod, Y. Altintas, E. Armarego, D. Dornfeld, I. Grabec, J. Leopold, B. Lindstrom, D. Lucca, T. Obikawa, Shirakashi, H. Sato, Present situation and future trends in modelling of machining operations progress report of the CIRP working group ‘modelling of machining operations’, *CIRP Ann.* 47 (1998) 587–626, [https://doi.org/10.1016/S0007-8506\(07\)63244-2](https://doi.org/10.1016/S0007-8506(07)63244-2).
- [2] F.W. Taylor, On the art of cutting metals, *Trans. ASME* 28 (1907) 31.
- [3] B.N. Colding, A three-dimensional, tool-life equation—machining economics, *J. Eng. Ind.* 81 (1959) 239–249, <https://doi.org/10.1115/1.4008313>.
- [4] D. Johansson, S. Hägglund, V. Bushlya, J.-E. Ståhl, Assessment of commonly used tool life models in metal cutting, *Procedia Manuf.* 11 (2017) 602–609, <https://doi.org/10.1016/j.promfg.2017.07.154>.
- [5] J.F. Archard, Contact and rubbing of flat surfaces, *J. Appl. Phys.* 24 (1953) 981–988, <https://doi.org/10.1063/1.1721448>.
- [6] T.N. Loladze, Of the theory of diffusion wear, *CIRP Ann.* 30 (1981) 71–76, [https://doi.org/10.1016/S0007-8506\(07\)60898-1](https://doi.org/10.1016/S0007-8506(07)60898-1).
- [7] E. Usui, T. Shirakashi, T. Kitagawa, Analytical prediction of cutting tool wear, *Wear* 100 (1984) 129–151, [https://doi.org/10.1016/0043-1648\(84\)90010-3](https://doi.org/10.1016/0043-1648(84)90010-3).
- [8] P.D. Hartung, B.M. Kramer, B.F. von Turkovich, Tool wear in titanium machining, *CIRP Ann.* 31 (1982) 75–80, [https://doi.org/10.1016/S0007-8506\(07\)63272-7](https://doi.org/10.1016/S0007-8506(07)63272-7).
- [9] X. Hong, Wear behaviour and wear mechanism of ceramic tools in machining hardened alloy steel, *Wear* 139 (1990) 439–451, [https://doi.org/10.1016/0043-1648\(90\)90061-E](https://doi.org/10.1016/0043-1648(90)90061-E).
- [10] B.M. Kramer, B.F. von Turkovich, A comprehensive tool wear model, *CIRP Ann.* 35 (1986) 67–70, [https://doi.org/10.1016/S0007-8506\(07\)61840-X](https://doi.org/10.1016/S0007-8506(07)61840-X).
- [11] Y. Huang, T.G. Dawson, Tool crater wear depth modeling in CBN hard turning, *Wear* 258 (2005) 1455–1461, <https://doi.org/10.1016/j.wear.2004.08.010>.
- [12] A. Malakzadi, B. Shi, P. Hoier, H. Attia, P. Krajinik, Physics-based approach for predicting dissolution–diffusion tool wear in machining, *CIRP Ann.* 69 (2020) 81–84, <https://doi.org/10.1016/j.cirp.2020.04.040>.
- [13] O. Gutnichenko, V. Bushlya, J. Zhou, J.-E. Ståhl, Tool wear and machining dynamics when turning high chromium white cast iron with pcBN tools, *Wear* 390–391 (2017) 253–269, <https://doi.org/10.1016/j.wear.2017.08.005>.
- [14] N. Ånmark, A. Karasev, P.G. Jönsson, The effect of different non-metallic inclusions on the machinability of steels, *Materials* 8 (2015) 751–783, <https://doi.org/10.3390/mater8020751>.
- [15] D. Nguyen, S. Tooptong, K.-H.H. Park, P. Kwon, Formation mechanism of alumina layer in protecting cubic boron nitride inserts in turning cast irons, *Int. J. Mach. Tool Manufact.* 153 (2020) 103539, <https://doi.org/10.1016/j.ijmachtools.2020.103539>.
- [16] J.-E. Ståhl, Requirements and potential for high performance cutting tools based on superhard phases in new applications Title, in: De Beers Diamond Conference Hosted by Warwick University, UK, 2016.
- [17] M. Olsson, F. Lenrick, R. M'Saoubi, H. Larsson, A. Markström, I. Petrusha, J.-E. Ståhl, V. Bushlya, Study of wear mechanisms of cemented carbide tools during machining of single-phase niobium, *Wear* 450–451 (2020) 203244, <https://doi.org/10.1016/j.wear.2020.203244>.
- [18] R. Lindvall, F. Lenrick, H. Persson, R. M'Saoubi, J.-E. Ståhl, V. Bushlya, Performance and wear mechanisms of PCD and pcBN cutting tools during machining titanium alloy Ti6Al4V, *Wear* (2020) 454–455, <https://doi.org/10.1016/j.wear.2020.203329>.
- [19] V. Bushlya, A. Bjerke, V.Z.Z. Turkevich, F. Lenrick, I.A.A. Petrusha, K.A. Cherednichenko, J.-E.E. Ståhl, On chemical and diffusional interactions between PCBN and superalloy Inconel 718: imitative experiments, *J. Eur. Ceram. Soc.* 39 (2019) 2658–2665, <https://doi.org/10.1016/j.jeurceramsoc.2019.03.002>.
- [20] S. Odelros, B. Kaplan, M. Kritikos, M. Johansson, S. Norgren, Experimental and theoretical study of the microscopic crater wear mechanism in titanium machining, *Wear* 376–377 (2017) 115–124, <https://doi.org/10.1016/j.wear.2017.01.104>.
- [21] V. Bushlya, F. Lenrick, J.-E. Ståhl, R. M'Saoubi, Influence of oxygen on the tool wear in machining, *CIRP Ann.* 67 (2018) 79–82, <https://doi.org/10.1016/j.cirp.2018.03.011>.
- [22] T. Aiso, U. Wiklund, M. Kubota, S. Jacobson, Effect of Si and Al additions to carbon steel on material transfer and coating damage mechanism in turning with CVD coated tools, *Wear* 368–369 (2016) 379–389, <https://doi.org/10.1016/j.wear.2016.10.011>.
- [23] J. Vleugels, O. Van Der Biest, Chemical wear mechanisms of innovative ceramic cutting tools in the machining of steel, *Wear* 225–229 (1999) 285–294, [https://doi.org/10.1016/S0043-1648\(98\)00362-7](https://doi.org/10.1016/S0043-1648(98)00362-7).
- [24] S. Giménez, O. Van der Biest, J. Vleugels, The role of chemical wear in machining iron based materials by PCD and PCBN super-hard tool materials, *Diam. Relat. Mater.* 16 (2007) 435–445, <https://doi.org/10.1016/j.diamond.2006.08.017>.
- [25] V. Bushlya, F. Lenrick, A. Bjerke, H. Aboulfadl, M. Thuvander, J.-E. Ståhl, R. M'Saoubi, Tool wear mechanisms of pcBN in machining Inconel 718: analysis across multiple length scale, *CIRP Ann.* (2021), <https://doi.org/10.1016/j.cirp.2021.04.008>.
- [26] G.J. Tennenhouse, F.D. Runkle, The effects of oxygen on the wear of tungsten-carbide-based materials, *Wear* 118 (1987) 365–375, [https://doi.org/10.1016/0043-1648\(87\)90078-0](https://doi.org/10.1016/0043-1648(87)90078-0).
- [27] J. Angseryd, H.-O.O. Andrén, An in-depth investigation of the cutting speed impact on the degraded microstructure of worn PCBN cutting tools, *Wear* 271 (2011) 2610–2618, <https://doi.org/10.1016/j.wear.2010.11.059>.
- [28] G.J. Tennenhouse, F.D. Runkle, The effects of oxygen on the wear of Si3N4 against cast iron and steel, *Wear* 110 (1986) 75–81, [https://doi.org/10.1016/0043-1648\(86\)90153-5](https://doi.org/10.1016/0043-1648(86)90153-5).
- [29] R.F. Silva, F.J. Oliveira, F.P. Castro, J.M. Vieira, Modeling of chemical wear in ferrous alloys/silicon nitride contacts during high speed cutting, *Acta Mater.* 46 (1998) 2501–2507, [https://doi.org/10.1016/S1359-6454\(98\)80034-7](https://doi.org/10.1016/S1359-6454(98)80034-7).
- [30] P.A. Dearmyrd, E.M. Trent, Wear mechanisms of coated carbide tools, *Met. Technol.* 9 (1982) 60–75, <https://doi.org/10.1179/030716982803285909>.
- [31] J.F.F. Archard, W. Hirst, The wear of metals under unlubricated conditions, *Proc. R. Soc. London Ser. A. Math. Phys. Sci.* 236 (1956) 397–410, <https://doi.org/10.1098/rspa.1956.0144>.
- [32] O. Hatt, H. Larsson, F. Giuliani, P. Crawforth, B. Wynne, M. Jackson, Predicting chemical wear in machining titanium alloys via a novel low cost diffusion couple method, *Procedia CIRP* 45 (2016) 219–222, <https://doi.org/10.1016/j.procir.2016.01.196>.
- [33] J.-O.J.-O. Andersson, T. Helander, L. Höglund, P. Shi, B. Sundman, L. Hoglund, P. Shi, B. Sundman, Thermo-Calc & DICTRA, computational tools for materials science, *Calphad* 26 (2002) 273–312, [https://doi.org/10.1016/S0364-5916\(02\)00037-8](https://doi.org/10.1016/S0364-5916(02)00037-8).
- [34] J.-E. Ståhl, *Metal Cutting: Theories in Practice*, SECO TOOLS, Fagersta, Sweden, 2012.
- [35] N.M. Major, S.T. Crawford, Elbow effusions in trauma in adults and children: is there an occult fracture? *AJR Am. J. Roentgenol.* 178 (2002) 413–418. <http://www.ncbi.nlm.nih.gov/pubmed/11804906>.
- [36] E.D. Doyle, J.G. Horne, D. Tabor, Frictional interactions between chip and rake face in continuous chip formation, *Proc. R. Soc. Lond. A. Math. Phys. Sci.* 366 (1979) 173–183, <https://doi.org/10.1098/rspa.1979.0046>.
- [37] X.-G. Lu, M. Selleby, B. Sundman, Implementation of a new model for pressure dependence of condensed phases in Thermo-Calc, *Calphad* 29 (2005) 49–55, <https://doi.org/10.1016/j.calphad.2005.04.001>.
- [38] S. Hampshire, H.K. Park, D.P. Thompson, K.H. Jack, α' -Sialon ceramics, *Nature* 274 (1978) 880–882, <https://doi.org/10.1038/274880a0>.
- [39] R. Riedel, I.-W. Chen, Ceramics science and technology, in: *Materials and Properties*, 2, Wiley, 2011.
- [40] W.-G. Seo, F. Tsukihashi, Thermodynamic and structural properties for the FeO–SiO₂ system by using molecular dynamics calculation, *Mater. Trans.* 46 (2005) 1240–1247, <https://doi.org/10.2320/matertrans.46.1240>.
- [41] V. Bushlya, J. Zhou, P. Avdovic, J.-E. Ståhl, Wear mechanisms of silicon carbide-whisker-reinforced alumina (Al₂O₃–SiCw) cutting tools when high-speed machining aged Alloy 718, *Int. J. Adv. Manuf. Technol.* 68 (2013) 1083–1093, <https://doi.org/10.1007/s00170-013-4899-8>.
- [42] G. Brandt, A. Gerendas, M. Mikus, Wear mechanisms of ceramic cutting tools when machining ferrous and non-ferrous alloys, *J. Eur. Ceram. Soc.* 6 (1990) 273–290, [https://doi.org/10.1016/0955-2219\(90\)90019-C](https://doi.org/10.1016/0955-2219(90)90019-C).
- [43] R. Reichelt, Scanning electron microscopy, in: P.W. Hawkes, J.C.H. Spence (Eds.), *Sci. Microsc.*, Springer, New York, NY, 2007, pp. 133–272, https://doi.org/10.1007/978-0-387-49762-4_3.
- [44] K.E. Lindgren, A. Kauppi, L.K.L. Falk, Development of matrix microstructure in polycrystalline cubic boron nitride ceramics, *J. Eur. Ceram. Soc.* 37 (2017) 3017–3026, <https://doi.org/10.1016/j.jeurceramsoc.2017.03.010>.
- [45] I. Gonzalez De Arrieta, T. Echaniz, R.B. Perez-Saez, M.J. Tello, I.G. de Arrieta, T. Echániz, R.B. Pérez-Sáez, M.J. Tello, Thermo-radiative and optical properties of a cutting tool based on polycrystalline cubic boron nitride (PCBN), *Mater. Res. Express* 3 (2016), 045904, <https://doi.org/10.1088/2053-1591/3/4/045904>.
- [46] M. Bacci da Silva, J. Wallbank, Cutting temperature: prediction and measurement methods—a review, *J. Mater. Process. Technol.* 88 (1999) 195–202, [https://doi.org/10.1016/S0924-0136\(98\)00395-1](https://doi.org/10.1016/S0924-0136(98)00395-1).
- [47] W.F. Ding, J.H. Xu, Y.C. Fu, B. Xiao, H.H. Su, H.J. Xu, Interfacial reaction between cubic boron nitride and Ti during active brazing, *J. Mater. Eng. Perform.* 15 (2006) 365–369, <https://doi.org/10.1361/105994906X108747>.
- [48] A.B. Ovako, Hybrid steel 55. https://steelnavigator.ovako.com/steel-grades/20n_icrmov24-20-7/, 2020 accessed July 1, 2020.